Die approbierte Originalversion dieser Diplom-/Masterarbeit ist an der Hauptbibliothek der Technischen Universität Wien aufgestellt (http://www.ub.tuwien.ac.at).

The approved original version of this diploma or master thesis is available at the main library of the Vienna University of Technology (http://www.ub.tuwien.ac.at/englweb/).

D I P L O M A R B E I T

Reproducibility of the HR-pQCT based FE-Analysis of the Distal Radius

ausgeführt zum Zwecke der Erlangung des akademischen Grades eines
Diplom-Ingenieurs
unter der Leitung von

Univ.Prof. Dipl.-Ing. Dr.techn. Philippe K. Zysset
Institut für Leichtbau und Struktur-Biomechanik, E317

eingereicht an der Technischen Universität Wien
Fakultät für Maschinenbau

von

Leopold Wagner
Sportplatzstr. 12
A-3362 Mauer

Wien, am 4th September 2010

D I P L O M A T H E S I S

Reproducibility of the HR-pQCT based FE-Analysis of the Distal Radius

presented for obtaining the academic degree of Diplom-Ingenieur
under the supervision of

Univ.Prof. Dipl.-Ing. Dr.techn. Philippe K. Zysset
Institute of Lightweight Design and Structural Biomechanics, E317

submitted at Vienna University of Technology
Faculty of Mechanical Engineering

by

Leopold Wagner
Sportplatzstr. 12
A-3362 Mauer

Vienna, 4th September 2010

Acknowledgements

I would like to thank Prof. Philippe K. Zysset for the strategic supervision of my thesis. He always had valuable suggestions and hints for me. I am deeply indebted to Dr. Peter Varga, who supported Prof. Zysset in supervising me. Most of all his Doctoral Thesis provided the baseline for this work and I could rely on him basically every day.

Special thanks also go to Dr. Dieter Pahr, the developer of `MedTool`, for his help on problems, regarding image processing and finite elements, Enrico Dall'Ara, who had useful hints for the specimen preparation, and Gerhard Schneider, who solved all my computer problems during this work. I would also like to thank Prof. Michael Pretterklieber from the Dept. of Applied Anatomy at the Medical University of Vienna for providing the specimens. Thanks also to Prof. Franz Kainberger and Julia Deutschmann, for further support with the XtremeCT at the Radiology Dept. of the Vienna General Hospital.

I would also like to thank my parents and grandparents, who made it possible for me to study free from worries. They always encouraged and supported me.

I owe my deepest gratitude to Martina, she helped me over the last one and a half years of my studying here in Vienna. She is my love and the person I can always rely on.

Abstract

High Resolution peripheral Quantitative Computed Tomography (HR-pQCT) based Finite Element (FE) analysis of the distal radius has the potential to become a future diagnostic tool for osteoporosis. When pathological processes or therapeutic effects shall be quantified, it is necessary to know the reproducibility of a diagnostic tool.

Six pairs of fresh frozen human cadaver forearms were scanned six times with the HR-pQCT system at the AKH Wien. The first series of the scans was selected as the Baseline (BL) and the following five represent the Follow Ups (FU). Next to the clinical region, currently investigated, (STD region) a second, distally shifted, region (MD region) and a third region, representing a combination of STD & MD (DS region), were analysed. Two modelling strategies, the micro FE (μFE) approach and the homogenized FE (hFE) method, were used to create the FE models of the three radius regions, respectively. In addition to the FE analysis, the bone mineral density (BMD) was evaluated from these HR-pQCT images. Image registration was performed on the five FU to find the corresponding BL images, and the whole analysis (BMD & FE) was repeated for these registered FU.

The MD region and the DS region were weaker, from both structural and material points of view, than the STD region. The reproducibility was quantified by precision errors. $PE_{\%CV}$ of the FU of STD, MD and DS regions was very good already at the unregistered stage. The reproducibility of all measures could be improved through image registration. Reproducibility was (1) generally better for the STD region than for the MD and DS regions, and (2) better for BMD measures than for μFE and hFE derived measures. The resulting reproducibility of all three regions was similar after the image registration for both μFE and hFE approaches (STD: $PE_{\%CV}$ >0.8%; MD: $PE_{\%CV}$ >1.5%; DS: $PE_{\%CV}$ >1.4%). Image registration introduced a shift in the FE results, μFE decreased and hFE increased.

A clear limitation of the present study came from the usage of cadaver forearms: patient motion was not included, so the obtained reproducibility represents a 'best case' scenario for the *in vivo* case. The reproducibility of the μFE and hFE analysis still needs to be investigated by an *in vivo* study to evaluate the effects of movement artefacts and finally obtain clinically relevant results.

Kurzfassung

Die, auf High Resolution periphäre Quantitative Computer Tomographie (HR-pQCT) basierte, Finite Elemente (FE) Analyse des distalen Radius hat das Potential eine zukünftige Diagnosemethode für Osteoporose zu werden. Es ist notwendig die Reproduzierbarkeit einer Diagnosemethode zu kennen, um Veränderungen als pathologische oder therapeutische Effekte zu quantifizieren.

Sechs Paare von Unterarmen wurden *in vitro* jeweils sechs mal mit dem HR-pQCT-System am AKH Wien gescannt. Die erste Serie von Scans wurde als Baseline (BL), die fünf folgenden als Follow Up (FU) definiert. Ausser der klinischen Region (STD Region) wurden noch eine zweite, distal verschobene, Region (MD Region) und eine dritte Region, welche sich aus STD & MD zusammensetzt, untersucht. Auf alle drei Regionen wurden jeweils zwei Modellierungszugänge angewandt: die micro FE (μFE) und die homogenized FE (hFE) Methode. Zusätzlich zur FE-Analyse wurde auch die Knochendichte aus den HR-pQCT-Bildern evaluiert. Um die BL Bilder in den FU Bildern wiederzufinden wurde Image Registration angewandt, und die gesamte Analyse (Knochendichte & FE) für diese registrierten FU wiederholt.

Die MD und die DS Region waren, aus struktureller und materieller Sicht, schwächer als die STD Region. Die Reproduzierbarkeit wurde mit Precision Errors ($PE_{\%CV}$) quantifiziert, welche bereits für die nicht registrierten FU sehr gering waren. Durch die Image Registration konnten die $PE_{\%CV}$ von allen Ergebnissen verringert werden. Die Reproduzierbarkeit war: (1) generell am besten für die STD Region, gefolgt von den MD und DS Regionen, und (2) besser für die Knochendichtemessung als für die μFE und hFE Ergebnisse. Schliesslich war die Reproduzierbarkeit, nach der Image Registration, ähnlich für die μFE und hFE Ergebnisse (STD: $PE_{\%CV}$ >0.8%; MD: $PE_{\%CV}$ >1.5%; DS: $PE_{\%CV}$ >1.4%). Die Image Registration verursachte allerdings eine Verringerung der absoluten μFE Ergebnisse und eine Erhöhung der hFE Ergebnisse.

Eine Beschränkung dieser Studie folgt aus der Verwendung von Unterarmen *in vitro*: Patientenbewegungen sind nicht inkludiert, die resultierende Reprozierbarkeit stellt daher ein 'best case' Szenario für den *in vivo* Fall dar. Die Reproduzierbarkeit der μFE und hFE Analyse muss also noch durch eine *in vivo* Studie untersucht werden, um die Effekte von Bewegungsartefakten zu bestimmen und zu klinisch relevanten Ergebnissen zu kommen.

Contents

Acknowledgements **1**

Abstract **2**

Kurzfassung **3**

List of Figures **6**

List of Tables **8**

1 Introduction **9**
1.1 Bone and Osteoporosis 9
1.1.1 The Radius 10
1.1.2 Osteoporosis and Fracture Risk 10
1.2 Diagnostic Tools 11
1.3 The Finite Element Method applied to Bone 11
1.4 Objectives and Outline 13

2 Methods **15**
2.1 Specimen Acquisition 15
2.1.1 Specimens 15
2.1.2 Specimen Preparation 16
2.2 HR-pQCT Scanning 17
2.2.1 The Scanning Procedure 17
2.2.2 Region Definition 19
2.3 Basic Image Processing 21
2.3.1 Rough selection of the radius by Graphical Objects (GOBJs) 21
2.3.2 BMD-scaling 23
2.3.3 Identification of the Radius within the Images 23
2.4 Micro FE Modelling and Analysis 24
2.4.1 Image Processing to create the μFE models 24
2.4.2 μFE Analysis 26
2.5 Homogenized FE Modelling and Analysis 29
2.5.1 Image Processing to create the hFE Models 29

2.5.2 hFE Analysis 36
2.6 Bone Densitometric Measurements 37
2.6.1 Bone Mineral Content (BMC) 37
2.6.2 Areal Bone Mineral Density (aBMD) 38
2.6.3 Volumetric Bone Mineral Density (vBMD) 38
2.7 Image Registration 38
2.8 Statistics 41

3 Results **44**
3.1 Baseline Results for all three Regions 44
3.2 Resulting Reproducibility and Improvement through Image Registration 47

4 Discussion **55**
4.1 Resulting Baseline Values 55
4.2 Reproducibility and its Improvement through Image Registration 59
4.2.1 Reproducibility of the Bone Density Measurements 60
4.2.2 Reproducibility of the FE-Analysis 62
4.3 Limitations 63
4.4 Outlook and Future Prospectives 65
4.5 Conclusions 65

List of Symbols **67**

Bibliography **69**

List of Figures

1.1 Hierarchical levels of the structure of cortical and trabecular bone; from [29] . . . 9

2.1 Flow chart of the study with: BL ... baseline; FU ... follow up; STD ... standard region; MD ... most distal region; DS ... double section region; BMD ... bone mineral density evaluation; μFE ... μFE analysis; hFE ... hFE analysis; . . . 15
2.2 Standard forearm fixation (from [6]) . . . 16
2.3 Specimen with veterinary gloves; left: each finger could be positioned correct; right: grasping of the 'handle' . . . 17
2.4 The three scanned 9.02mm regions, region B corresponds to the clinical region . . . 18
2.5 Typical 2D scout views showing the position of the StdRefLin (111.194) and the scanned 27.56 mm section of the distal radius (left), and the position of the MostDistRefLin (115.308), not touching the lunate fossa (right). The distance between the StdRefLin and the MostDistRefLin here results in 115.308 - 111.194 = 4.114 mm . . . 19
2.6 Location of the Standard Region (STD), the Most Distal Region (MD) and the Double Section Region (DS), adapted from [36] . . . 20
2.7 GOBJs on reference slices - first and last slice (solid black), interpolated GOBJs (dotted black) and 'key'-GOBJ (solid red); modified from [2] . . 21
2.8 GOBJ on Slice 1 (left); Interpolated GOBJ (center); 'key'-GOBJ on MostDistRefLin position (right) . . . 22
2.9 GOBJ on 'key'-slice within the distal radio-ulnar joint (left); the articular gap is represented by only a few voxels (right) . . . 22
2.10 A slice of a BMD-scaled image (left) and the corresponding slice of the 'outer' mask after the *-fill* algorithm (right) . . . 24
2.11 A slice of a BMD-scaled Image (left) and the corresponding slice of the segmented image (right) . . . 25
2.12 Corresponding slices of the 'outer'- (left), the 'inner'- (center) and the 'thickness' mask (right) . . . 26

2.13 Corresponding slices of the segmented image (left), the 'thickness' mask (center) and the final image for the μFE input (right) with cortical (white) and trabecular (grey) bone voxels 26
2.14 Cortical (yellow) and trabecular elements (white) 27
2.15 Boundary conditions for the uni-axial compression test for a typical MD region; from [36] 28
2.16 Contours used for the triangulation of a DS Region; the most distal contour is not one single closed line 29
2.17 Severe problems with triangulation for a triangulated MD region 30
2.18 Initial triangular mesh (left) and the corresponding corrected mesh (right) of a STD region 30
2.19 The resulting 3D mesh with trabecular (blue) and cortical (red) elements 31
2.20 Volume fraction distribution of the whole grid (left) and assignment of these quantities to the elements of the trabecular compartment (right) 33
2.21 Fabric orientation of each trabecular element (right): red is major direction 34
2.22 Wire frames of the cortex-elements with the corresponding material coordinate systems of each element 35

3.1 Mean±SD of the BMC differences [%] between BL and unregistered FU (blue) and registered FU (red) for STD (left), MD (middle) and DS regions (left) 48
3.2 Mean±SD of the $F_{ult}^{\mu FE}$ differences [%] between BL and unregistered FU (blue) and registered FU (red) for STD (left), MD (middle) and DS regions (left) 48
3.3 Mean±SD of the F_{ult}^{hFE} differences [%] between BL and unregistered FU (blue) and registered FU (red) for STD (left), MD (middle) and DS regions (left) 49
3.4 Comparison of the differences of %CV (μFE F_{ult}) before and after the image registration and MS_{BONE} STD regions (left) and MD regions (right) 50

List of Tables

3.1 Baseline results for STD & MD: mean±SD; mean±SD of the differences between STD & MD; baseline results for DS; mean±SD of the differences between STD & DS; [p] differences between regions are significant; [x] differences between hFE and μFE are significant; - not comparable 45

3.2 Pearson's correlation coefficients (R^2, left) and Concordance correlation coefficients (CC, right) of μFE and hFE comparison; STD standard region, MD most distal region, DS double section region 46

3.3 Pearson's Correlation Coefficients R^2 of the comparison between bone mineral density and FE results, bold numbers indicate high correlations (R^2 >0.8) 46

3.4 Differences between baseline and follow up for STD BMC in [%]); right: specimen mean±SD; bottom: measurement mean±SD; bold numbers on right bottom: overall mean±SD 47

3.5 Differences (in [%]) between BL and unregistered/registered FU and between unregistered and registered FU; hFE DS Follow Ups not calculated 51

3.6 $PE_{\%CV}$ of the bone mineral density measures for unregistered/registered FU of the STD, MD and DS Regions; * 95%CI of unreg. and reg. FU do not overlap 52

3.7 $PE_{\%CV}$ of the bone mineral density measures for unregistered/registered FU of the STD, MD and DS regions; hFE FU for DS not calculated; * 95%CI of unreg. and reg. FU do not overlap 52

3.8 LSC of bone mineral density and FE results for unregistered and registered STD, MD and DS regions: absolute values and percentage (in brackets); absolute values calculated with the mean of the unregistered or registered FU, respectively; hFE DS Follow Ups not calculated 53

3.9 ICCs and their 95% confidence intervals for all measured/calculated parameters of STD, MD and DS regions; hFE FU for DS not calculated; * 95%CI of unreg. and reg. FU do not overlap 54

Chapter 1

Introduction

1.1 Bone and Osteoporosis

Bone is a natural composite material with a hierarchical structure (see Fig. 1.1). It constitutes from a fibrous component - collagen, a mineral phase - Hydroxyapatite (HA) and water [29]. The macrostructure can be separated into cortical bone and trabecular bone. Cortical bone is rather dense, with a porosity less than 10%, and it can be found in the outer shell of almost every bone, especially in the diaphysis of long bones. Trabecular bone, due to its appearance also called spongious bone, has a very high porosity (>70%). It can be found in the epiphysis of long bones and in the center of flat bones.

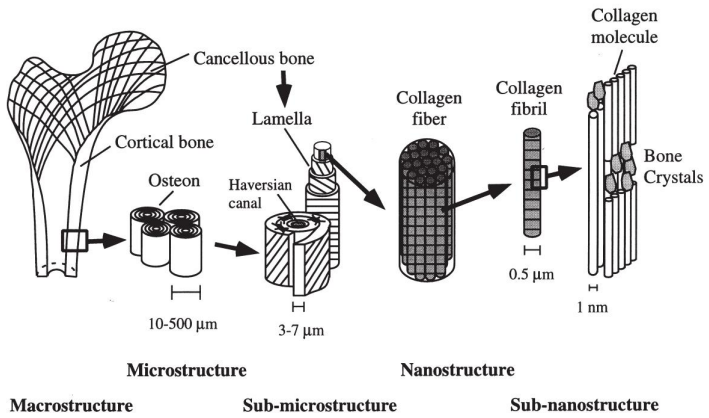

Figure 1.1: Hierarchical levels of the structure of cortical and trabecular bone; from [29]

The first level of structural hierarchy in cortical bone are the osteons, with their Haversian canals in the middle. The osteons constitute from bone lamellae,

which also form the individual trabeculae. The following hierarchical levels, down to the collagen molecules and HA crystals themselves, can be seen on Figure 1.1.

1.1.1 The Radius

The radius is, together with the ulna, the major long bone of the human forearm [15]. Like every long bone, the radius consists of a diaphysis or bone shaft (*corpus radii*), and a distal and proximal epiphysis (*distal & proximal extremity*). The distal extremity is larger than the proximal one and it provides two articular surfaces: one for the carpus (distal end) and one for the ulna (medial side). The radio-carpal articular surface is triangular, concave, smooth and divided by a slight anterior-posterior ridge into two parts: the lateral part of the articular surface articulates with the scaphoid bone and the medial part with the lunate bone.

1.1.2 Osteoporosis and Fracture Risk

The bony architecture and mineralisation undergo permanent changes due to the remodelling process. The cellular compartments maintain the bone structure: osteoblasts are responsible for deposition of bone material and osteoclasts perform bone resorption. These cellular activities have to be kept in equilibrium. Unbalance of this equilibrium, i.e. increased bone resorption, leads to a loss of total bone mass and a decreased mineralisation of the bone tissue. Depending on the severity of these effects, different pathological conditions can be diagnosed. Osteoporosis, the most severe case, is characterized as a skeletal disease, leading to a loss in total bone mass and a secondary deterioration of the bone micro-structure [1]. The wrist is, besides the hip and the spine, most affected by osteoporosis related fractures. Wrist fractures, e.g. of Colles' or Smith's type, early occur during the development of osteoporosis and are often reported in patients, not diagnosed to be osteoporotic before. Therefore the wrist is suitable for the diagnosis.

The treatment of osteoporosis related fractures charges the public health systems throughout the world with millions of Euros every year. With the shift of the population profile to higher ages in the upcoming decades, these costs are expected to increase rapidly, e.g. Europe: 32 billion Euros in 2025 [28].

1.2 Diagnostic Tools

The current diagnostic standard tool for osteoporosis is Dual Energy X-Ray Absorptiometry (DXA). It determines the areal Bone Mineral Density (aBMD). Mineralization has a strong influence on bone strength, but also the bone microstructure contributes to the bone strength. The deterioration of the bony architecture can not be depicted by DXA, relying on 2D-X-Ray images.

Quantitative Computed Tomography (QCT) offers the possibility to acquire 3D images and 3D bone mineral density measures like bone mineral content (BMC) or volumetric bone mineral density (vBMD). To obtain detailed images, i.e. to be able to resolve individual trabeculae, the spatial resolution of a QCT-scanner must be smaller than the thickness of a trabeculae. Therefore micro-CT (μCT) scanners were developed (e.g. μCT40, Scanco Medical AG, Switzerland). These scanners have the disadvantage that only small bone samples can be scanned, thus *in vivo* scanning of human bones is not possible. To be able to scan at least peripheral sites of the human body, e.g. the distal radius or the distal tibia, with a resolution that is sufficient to resolve single trabeculae, High Resolution peripheral Quantitative Computed Tomography (HR-pQCT) was developed [20] (e.g. XtremeCT, Scanco Medical). These scanners allow peripheral sites of the human body (distal radius, distal tibia) to be scanned *in vivo* with a nominal resolution of 82μm. A limitation of this technique is that only regions of 9mm length are assessable at once. A clinical region (later referred as standard region) was excessively investigated before (e.g. [36], [6], [22]) and distally shifted (most distal region) and enlarged regions were also investigated (e.g. [36]).

1.3 The Finite Element Method applied to Bone

The strategy of structural Finite Element Analysis can be, for a linear analysis, summarized as: (1) subdivide the geometrical model of a structure into small parts (elements) of finite size, (2) set a stress-strain relationship, e.g. described by a constitutive law, e.g. Equation 1.1),

$$\mathbf{E} = \mathbb{E}\mathbf{S} \tag{1.1}$$

(with $\mathbf{E}$ as the 2nd order Green-St Vernant material strain tensor, $\mathbb{E}$ as the 4th order compliance tensor and $\mathbf{S}$ as the 2nd order Piola-Kirchhoff 2 material stress tensor), (3) assemble these local relationships to a global equation system (e.g.

Equation 1.2),

$$\mathbf{KU} = \mathbf{F} \tag{1.2}$$

(with $\mathbf{K}$ as the global stiffness matrix, $\mathbf{U}$ as the nodal displacements and $\mathbf{F}$ as the nodal forces) (4) apply constraints of force and/or displacement type - boundary conditions - to chosen sets of nodes and (5) solve the global equation system to satisfy equilibrium. The results can then be interpreted in post-processing steps. For further details and the structure of a non-linear finite element analysis see e.g. Bathe [5].

In case of the Finite Element Analysis of a bony structure, unlike to classical mechanical problems, usually there is no geometrical input from CAD/CAE systems available. The structural information about the bone sample can only be acquired by medical imaging methods, like the above mentioned QCT or HR-pQCT. Depending on the image resolution available, different approaches of finite element modelling of a bony structure are used.

Typical resolutions of μCT scanners range from 5 to 30μm. μCT based modelling can therefore resolve individual trabeculae can be resolved in the image by several voxels. These voxels are then converted into hexahedral elements [35]. Homogeneous isotropic material properties are applied to all elements. These micro finite elements models (μFE) can represent the structure in detail, but they typically contain millions of elements [4]. These models therefore require outstanding computational resources and special purpose finite element solvers and additionally the analysis is usually limited to a linear analysis.

If there are only image resolutions >100μm available, single trabeculae cannot be resolved. Here larger elements are used and the material properties are homogenized within these elements, e.g. material properties scaled with the bone mineral density [18]. These homogenized finite elements models can represent the same structure, e.g. a distal radius section, with only several thousand elements, but do not contain any structural information.

Another homogenization method was developed based on morphology-elasticity relationships by Zysset & Curnier [40], recently reviewed by Zysset [39]. There morphological information, in form of an orientation distribution function (ODF), acquired by e.g. the mean intercept length method (MIL) [38], and a bone density parameter (volume fraction), must be provided. These homogenized finite element models (hFE) contain the bony micro-architecture, but do also consist of several

thousand elements only (see Section 2.5.2 or [36]).

1.4 Objectives and Outline

The HR-pQCT based finite element analysis of the distal radius has the potential to become a future diagnostic tool for osteoporosis [3], [20]. When a change of any parameter of bone quality shall be quantified, it is mandatory to know the reproducibility error of the measurement and the following analysis procedure itself. Only then it can be differentiated, whether the observed changes lie in a range where they may be quantified as significant, e.g. least significant change (LSC) [9], [17], or they just lie within the reproducibility error.

A study on reproducibility needs consecutive HR-pQCT scans of human forearms, i.e. a first baseline scan and then consecutive follow up scans. The effective radiation dose for scanning one 9mm region of the distal radius was reported to be 3μSv. In the present study the scanned region was extended to three 9mm regions (see 2.2.2), i.e. roughly 3cm of the distal radius were scanned. The problem with an *in vivo* volunteer study would arise from the increased radiation dose, due to the enlarged scanned region, and the schedule for the repeated scans, which were performed within only three weeks (see 2.2.1). Volunteer patients would be exposed to an increased radiation dose multiple times.

To still be able to keep close to the clinical situation, although performing an *in vitro* study, intact human cadaver forearms were used. The positioning of the forearm in the scanner cast could be simulated, closely to the clinical procedure. Also the soft tissue around the radius was still present, which may influence the CT-measurements. The use of cadaver forearms lead to a limitation of the present study: patient motion is not included. Errors induced by patient motion are a part of the reproducibility of HR-pQCT based measurements/analyses. So in the present study only the repositioning errors and the errors from the procedures, i.e. from HR-pQCT scanning to the bone mineral density measurement or the finite element modelling and analysis, are evaluated.

The analysis included bone mineral density measurements and μFE as well as hFE analysis of three regions of the distal radius. The baseline image was identified on the follow up images, using 3D image registration methods. The novel aspect about image registration comes from the enlarged scanned region, making 100% common regions of baseline and follow up possible (compare to [22]).

The goals of this study could be summarized:

- What is the reproducibility of the bone mineral density measures (BMC, vBMD, aBMD) and the μFE and hFE derived measures (K, F_{ult}, E_{app}, σ_Y)?
- Can the reproducibility of these measures be improved by the aid of the image registration?

and

- Do the bone mineral density measures and the μFE and hFE derived measures fit to results in literature?
- What are the differences of these measures due to different regions?
- Do hFE derived measures correspond to those from the μFE analysis?

These questions will be answered in the following Chapters. Chapter 2 will describe

- Specimen preparation and HR-pQCT scanning
- Image processing
- Measurement of Bone Mineral Density
- Finite Element modelling and analysis
- Statistical tools for the data analysis

Chapter 3 will present the baseline results as well as resulting reproducibility of the bone mineral density measures and the results of the μFE and hFE derived measures and also the influence of the image registration. In Chapter 4 these results will be discussed, as well as limitations of the present study and an outlook, based on these limitations, is given.

Chapter 2

Methods

The structure of the present study can be seen on Figure 2.1. The BMD evaluation and FE analysis were repeated for the three defined regions of the distal radius.

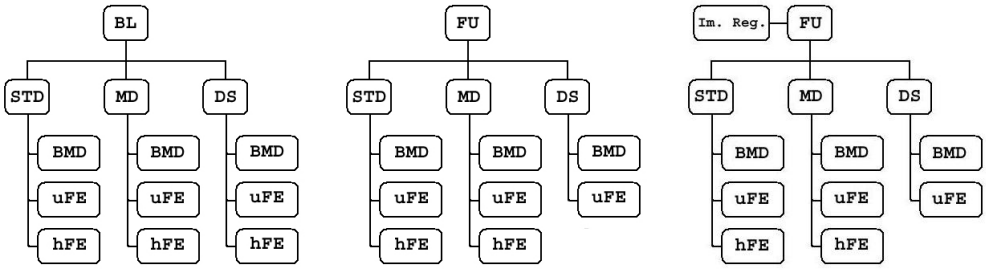

Figure 2.1: Flow chart of the study with: BL ... baseline; FU ... follow up; STD ... standard region; MD ... most distal region; DS ... double section region; BMD ... bone mineral density evaluation; μFE ... μFE analysis; hFE ... hFE analysis;

2.1 Specimen Acquisition

2.1.1 Specimens

Twelve human cadaver forearms from 6 individuals, who donated their bodies to the Center of Anatomy and Cell Biology/Dept. of Applied Anatomy at the Medical University of Vienna, were obtained. All procedures were performed in full agreement with the ethical regulations of the Medical University of Vienna. Four of the donors were female, two were male, mean age was 78 $\pm$ 14 years (min/max: 59/96 years). The forearms were dissected at the elbow. The proximal ends of the radius and the ulna were kept completely with their articular cartilage, only

the joint capsule and the ligaments at the elbow were removed. Each specimen was labelled with a specific sample ID, for recognition during the follow up scans, indicating year of birth, sex and side.

2.1.2 Specimen Preparation

To ensure that the HR-pQCT system (XtremeCT, Scanco Medical AG, Switzerland) did not get biologically contaminated, each forearm had to be sealed, e.g. packed into a hermetically sealed bag. In order to keep as close to the clinical procedure as possible, the standard forearm fixation of the XCT had to be used (see Fig. 2.2). It can be seen that it was mandatory to bend the fingers and that at least the thumb could be moved separately from all other fingers. Only then it could be ensured that the hand could grasp the 'handle' (green 'handle' in Figure 2.2 and Figure 2.3 left) of the forearm fixation.

Figure 2.2: Standard forearm fixation (from [6])

Grasping could not be performed if the arms were put into bags, where the fingers could not be moved individually. To ensure the possibility to grasp, the arms were put into veterinary gloves. These gloves could cover the whole arm up to the shoulder, so they could be wrapped together and knotted right after the elbow. These veterinary gloves had a low attenuation coefficient, close to the attenuation of plastic. Even multiple layers of these gloves were not thought to have major effects on the final image quality. It showed that putting each and every finger into the corresponding 'glove-finger' was very difficult. Finally this could be managed only for one pair of arms (see Figure 2.3 right). All other arms were put in such a way that at least the thumb and, in most of the cases, the second finger were put into the corresponding 'glove-finger'. To ensure more safety for all following manipulations, each forearm was put into two more gloves, resulting in three glove-layers over all. All arms were stored frozen at -20°C at

the Micromechanics Laboratory at the Vienna University of Technology between all manipulations.

Figure 2.3: Specimen with veterinary gloves; left: each finger could be positioned correct; right: grasping of the 'handle'

Thawing the forearms six times was supposed not to be possible due to the putrefaction process, continuing after each thawing. This was a result from the decision to keep the surrounding soft tissue. To save thawing/freezing procedures, each specimen was scanned twice every scheduled scanning at the Vienna General Hospital (AKH Wien).

Another problem were the biological fluids (blood and cellular & extracellular water), which came out of the soft tissue of each forearm after each thawing. Some specimens had to be re-opened prior to the second and third scheduled scanning to pour out these fluids. These forearms were covered additional veterinary gloves each because the inner - no more closed - glove layer was kept to facilitate the attachment of the new gloves. These additional gloves were not thought to have an effect on the image quality. Still the results of these two specimens had to be checked, whether this suggestion was justified.

2.2 HR-pQCT Scanning

2.2.1 The Scanning Procedure

Each specimen was scanned six times with the XtremeCT (XCT) at the Radiology Department of the General Hospital Vienna. The arms were scanned twice at every scheduled scanning (Baseline & Follow Up 1; Follow Up 2 & Follow Up 3; Follow Up 4 & Follow Up 5). Prior to all six scanning rounds, the standard daily

quality check QC1-Daily, using the standard Scanco Phantom, was performed to check whether the measured HA density was in the range recommended by the manufacturer.

The scanning was performed using the clinical *in vivo* standard scanning protocol: 60kVp effective energy, 901mA x-ray tube current, 100ms integration time, 2048 x 2048 pixels image matrix and 82μm nominal spatial isotropic resolution.

Compared to this clinical *in vivo* standard scanning procedure, a larger region of the distal radius had to be scanned to capture all regions of the distal radius to be analysed. Another 9mm region - region C in Fig. 2.4 - was scanned in order not to lack parts of the standard region after the image registration. Altogether three consecutive 9.02mm (110 slices) sections were scanned, resulting in a 27.06mm (330 slices) region of the distal radius (see Fig. 2.4). The first section (A) started 0.5 mm proximal to the standard reference line (StdRefLin), the second section (B) started 9.5 mm proximal to the StdRefLin. This position represents the standard region (clinical region). The third section (C) started proximal to the second section, 18.5 mm proximal to the StdRefLin. Total scanning time was approximately 9 minutes.

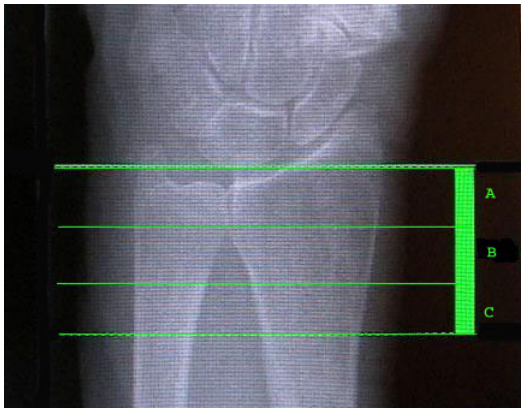

Figure 2.4: The three scanned 9.02mm regions, region B corresponds to the clinical region

To locate the reference lines for the scanning, a scout view was performed. The scout view is a 2D X-ray of the distal forearm, showing the distal epiphyses of the ulna and the radius and the carpal bones (Figure 2.4, 2.5). Within this scout view, the reference lines for the scanning procedure were positioned.

2.2.2 Region Definition

The regions, which were analysed in the following, had to be defined. The location of the standard region (STD) was defined according to the clinical standard *in vivo* protocol of the Scanco XCT, consisting of 110 slices with 82μm distance and leading to a 9.02 mm Region [20]. The standard reference line (StdRefLin) was set to the plateau between the scaphoid fossa and the lunate fossa of the distal radius (see Fig. 2.5 left). The STD region started 9.5 mm proximal and ended 18.5mm proximal to the StdRefLin (see also Fig. 2.6).

Several studies reported a region that is shifted in distal direction and has decreased mechanical properties and bone mineral density, e.g. [24], [36], [22]. The location of this most distal region (MD) was defined differently than reported before by Varga [36], where the images were checked slice by slice to find the first image slice containing only trabecular bone in the interior (personal communication from the author). In the present study the position of the most distal reference line (MostDistRefLin) was directly identified already on the scout view (see Fig. 2.5 right), just as it might be done in a clinical application of this MD region. In order to relocate the MD region within the scanned image, the distance D between the StdRefLin and the MostDistRefLin was determined.

$$D = MostDistRefLin - StdRefLin \tag{2.1}$$

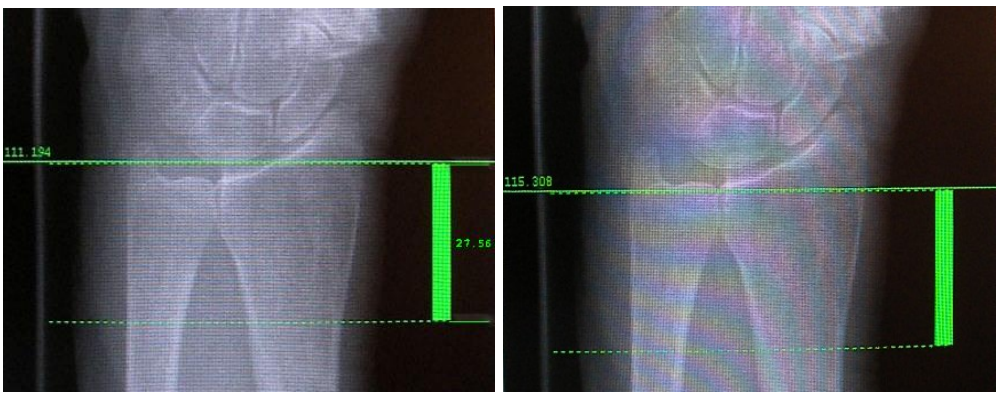

Figure 2.5: Typical 2D scout views showing the position of the StdRefLin (111.194) and the scanned 27.56 mm section of the distal radius (left), and the position of the MostDistRefLin (115.308), not touching the lunate fossa (right). The distance between the StdRefLin and the MostDistRefLin here results in 115.308 - 111.194 = 4.114 mm

The MostDistRefLin position could not be measured directly in some scans of

the largest specimens. The MostDistRefLin position was measured by the lower (dotted) line (Figure 2.5), being the proximal end of the scanned region in the reference line selection tool, and 27.56 mm was added to this value. If not even the StdRefLin could be captured, the specimen was repositioned.

Distal radius fractures do not entirely occur localized either within 9mm regions of the distal radius, like the STD or the MD region. Spadaro et.al. reported distances between the fractures and the radial styloid varying from 13 and 24mm [33], Eastell et.al. reported distances of 22±4mm [11]. A larger region of the distal radius might be mandatory, to cover the complete spectrum of fracture patterns. With the XtremeCT only 9.02mm can be scanned at once and this scanning requires approximately 3 minutes. It will be difficult to scan adjacent regions at once, without patient motion. Therefore double section regions (DS) were defined as a combination of the STD and the MD regions, ranging from the MostDistRefLin to the last slice of the STD region in proximal direction (see Fig. 2.6). These DS regions may be combined from images of the corresponding STD and MD regions in the clinical application. The STD and MD regions can be scanned separately and then the overlapping parts of the STD and MD regions can be used in an image registration step, to combine these two to the desired DS region.

An overview of all defined regions can be seen on Figure 2.6.

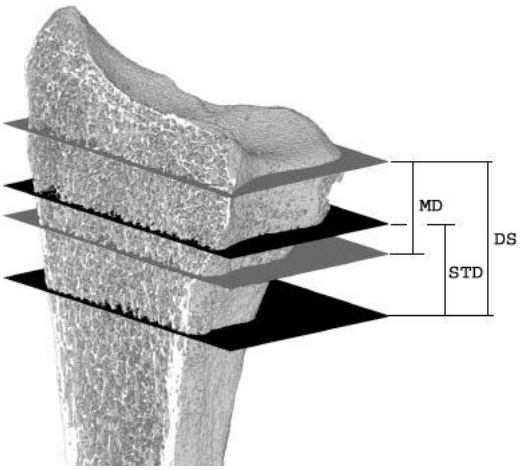

Figure 2.6: Location of the Standard Region (STD), the Most Distal Region (MD) and the Double Section Region (DS), adapted from [36]

There landmark for the STD region can be recognized well in the follow up scans. The landmark of the MD region is not so easy to detect. Therefore the

variance of all resulting measures of the MD regions - and also DS regions - were expected to be higher, compared to those of the STD regions.

2.3 Basic Image Processing

2.3.1 Rough selection of the radius by Graphical Objects (GOBJs)

The first step of the image processing was the selection of the volume of interest (VOI), in which the radius could be found. The VOI was defined by a set of graphical objects, i.e. one GOBJ in each slice of the HR-pQCT-image. The 3D-shape of the VOI can be defined by either drawing GOBJs on all consecutive slices or by creating a 'hull' between any two slices. This is done by an interpolation of missing GOBJs in between two hand-drawn GOBJs, called 'morphing' [2]. GOBJs were then drawn on the first and last slice and on some 'key'-slices in between (Figure 2.7).

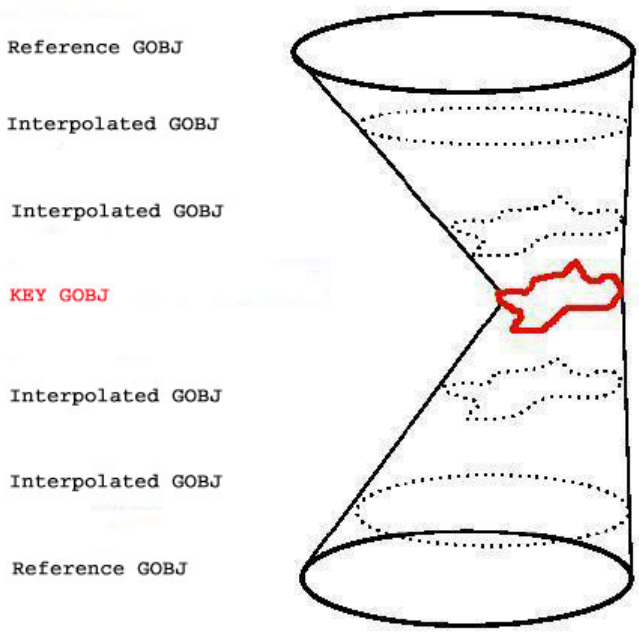

Figure 2.7: GOBJs on reference slices - first and last slice (solid black), interpolated GOBJs (dotted black) and 'key'-GOBJ (solid red); modified from [2]

These 'key'-slices were located at the proximal end of the lunate fossa, being the position of the MostDistRefLin, and the distal and proximal borders of the distal radio-ulnar joint (Figure 2.8). The articular joint gap between the radius

and the ulna in the distal radio-ulnar joint was the most critical part of contouring the image, because in some images the width of this articular gap was only in the range of a few voxels (see Fig. 2.9).

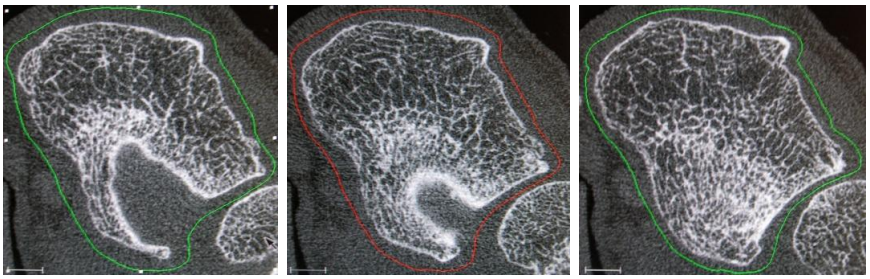

Figure 2.8: GOBJ on Slice 1 (left); Interpolated GOBJ (center); 'key'-GOBJ on Most-DistRefLin position (right)

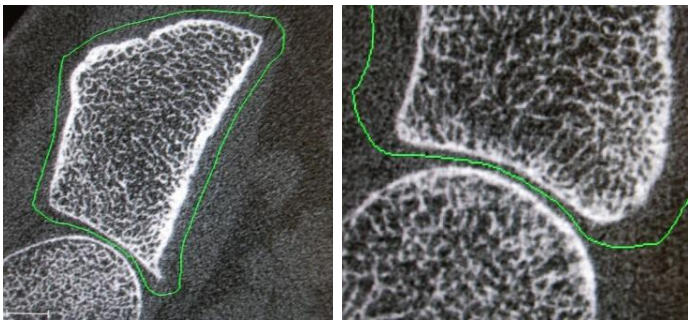

Figure 2.9: GOBJ on 'key'-slice within the distal radio-ulnar joint (left); the articular gap is represented by only a few voxels (right)

The resulting VOI could be shrinked automatically, based on grey-scale values, until the boundaries of the VOI get in contact with the cortical shell of the radius. This procedure works relatively well for good image quality and an intact cortical bone shell. If this is not the case, the VOI does no longer contain the whole bone structure, i.e. some parts of the cortical shell and also some trabecular bone structure can be lost [8]. Because of the image quality and the thin cortical bone shell at the distal radius, the automatic contour finding algorithm was not used. Thus the entire cortical bone shell was kept but also the surrounding soft tissue was included in the images and had to be removed afterwards.

The CT-images were then masked with these GOBJs and bounding-boxes were identified and cropped, using the IPL-software package at the XCT, to reduce memory requirements for image processing.

2.3.2 BMD-scaling

The voxel data of the raw HR-pQCT-images was given in native units, being 'scaled' linear attenuation coefficients (μ). The grey value of each voxel was not stored in μ, which would have been a float between $\sim$ -1.0 and 3.0, but multiplied with a scaling factor of 8192, in order to be able to store the data as integer, and reduce the disk space needed. To get back to linear attenuation, all voxel data had to be divided by this scaling factor. Then the data had to be converted into Bone Mineral Density (BMD) [mg/cm^3] by a calibration law (Eq. 2.2) included in the XCT. This calibration law was checked with scanning the phantom (QC1-Daily).

$$BMD = \mu * 1466.5 - 360.5 \tag{2.2}$$

This theoretically should give values up to $1200mg/cm^3$, representing density of pure Hydroxyapatite [6]. Negative densities, representing image artefacts or fat tissue in the bone marrow [14], were found as well as densities above $1200mg/cm^3$, representing again image artefacts or hyper-mineralized bone tissue. To reduce noise in the grey-scale values of the HR-pQCT images, in a first step all voxel data was limited to values from -200 mg/cm^3 to 1200 mg/cm^3, all data above and below these limits was set to these limits.

2.3.3 Identification of the Radius within the Images

A first rough selection of the radius within the HR-pQCT images was already performed by the GOBJs, but the images still contained the surrounding soft tissue. This soft tissue had to be from the images before the segmentation. The identification of the radius was performed by the *fill* algorithm with the *-out* option, described by Pahr [26] and implemented in `MedTool`. A grid of rays is passed through a grey-scale image from a given direction and from the opposite direction until they hit voxels with a grey-value above a given threshold. All voxels on the ray-path between these detected voxels are set to 1, all outside to 0. The rays are passed through the image from 7 directions and in such a way that each voxel is hit only once for each direction. All data from the 7 directions is added. The resulting image has voxel-values from 0 to 7, depending from how many directions one voxel is detected as bone voxel (for further details see [26]). In the current study 6 directions showed the best results, so all voxels with values 6 or 7 were kept and the image was stored as the 'outer' mask. As basis for the creation of the 'outer' masks the BMD-scaled images were used, therefore the threshold had to be

given in BMD-scales [mg/cm^3]. Prior to all these steps a Gaussian filtering with radius=2, support=1.2 was performed on the BMD-scaled images to increase the signal-to-noise ratio. An example of a BMD-scaled image and the corresponding 'outer' mask is shown on Figure 2.10.

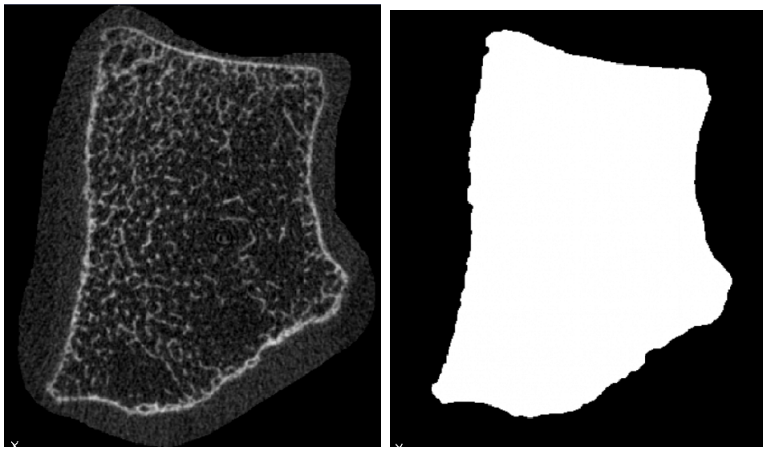

Figure 2.10: A slice of a BMD-scaled image (left) and the corresponding slice of the 'outer' mask after the *-fill* algorithm (right)

The raw HR-pQCT images were masked with these 'outer' masks, i.e. all voxel data outside the outer cortex contour was set to 0.

2.4 Micro FE Modelling and Analysis

2.4.1 Image Processing to create the μFE models

The raw HR-pQCT images of the STD, MD and DS regions were converted into μFE models. Therefore the external contour radius was identified as well as the inner contour. Then the image was segmented, subdivided into trabecular and cortical bone regions (only for computational reasons) and finally all 'bone' voxels were converted into hexahedral finite elements.

Image Segmentation

The raw HR-pQCT images were not masked with these 'outer' masks immediately, they were segmented first. The segmentation of HR-pQCT images with the present resolution of 82μm was a delicate task because the resolution lay in the same order of magnitude as the thickness of a typical trabeculae. A single level

threshold based segmentation [30] would lead to a loss of mostly volume fraction and also connectivity within the structure and in the following to a decrease of the mechanical and bone mineral density properties. A Laplace-Hamming filtering procedure was used to preserve the trabecular architecture [21] that is also used in the standard evaluation protocol embedded in the XtremeCT. After this filtering was applied and a global threshold of 40% of the maximum grey-scale intensity was set (see Fig. 2.11). The segmented images were cleaned from unconnected regions to avoid numerical problems in the following μFE analysis.

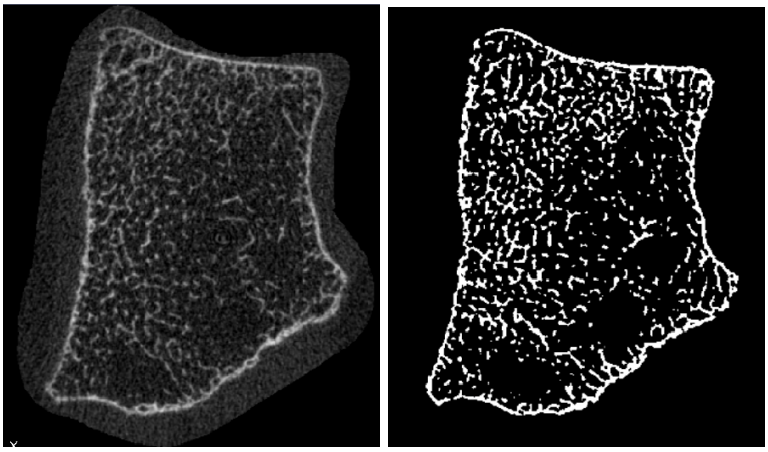

Figure 2.11: A slice of a BMD-scaled Image (left) and the corresponding slice of the segmented image (right)

Separating the cortical shell from the trabecular core of the Radius Regions

In order to evaluate of the ultimate force, using a failure-safety-factor, the μFE model, due to computational reasons only, had to consist of two types of elements. It was chosen to create these two sets of elements according to the two types of bone tissue, i.e. cortical elements and trabecular elements, because this separation was needed in the following homogenized FE modelling anyway. To fulfil this requirement the *fill* algorithm was used once again. Prior to this the raw images were filtered with the same Gaussian filter mentioned before (radius=2, support=1.2) and then masked with the 'outer' masks. Then the *fill* algorithm was used with the *in*-option [26] and the resulting image was the corresponding 'inner' mask, i.e. the inner contour of the cortical bone shell. This 'inner' mask was subtracted from the 'outer' mask to get the 'thickness' mask, representing all

cortical bone voxels (see Fig. 2.12).

'outer' - 'inner' = 'thickness'

Figure 2.12: Corresponding slices of the 'outer'- (left), the 'inner'- (center) and the 'thickness' mask (right)

This 'thickness' mask was added to the segmented binary image to get two different sets of voxels: cortical voxels and trabecular voxels (see Fig. 2.13 & 2.14).

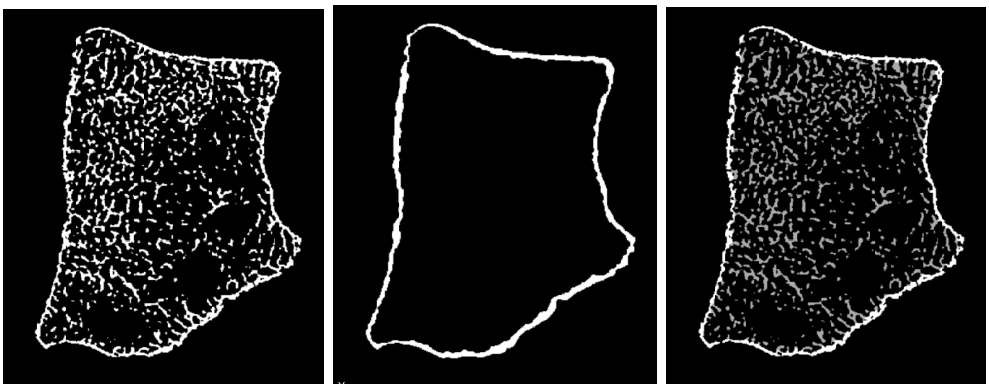

Figure 2.13: Corresponding slices of the segmented image (left), the 'thickness' mask (center) and the final image for the μFE input (right) with cortical (white) and trabecular (grey) bone voxels

2.4.2 μFE Analysis

All cortical and trabecular bone voxels of the final 3D-images were converted to linear (8-noded) hexahedral continuum elements, according to the direct voxel conversion approach by van Rietbergen et.al. [35]. Homogeneous isotropic mate-

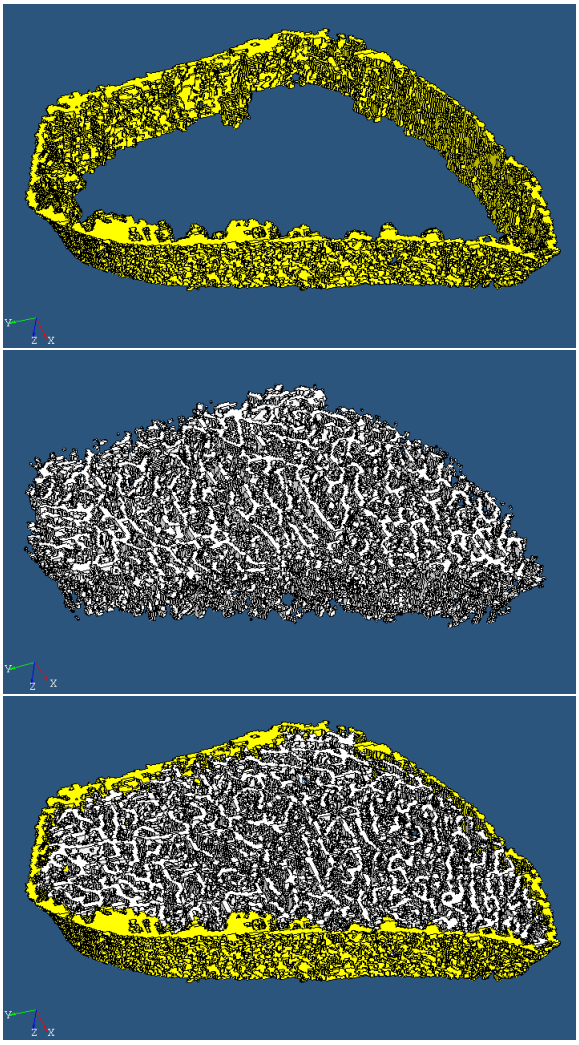

Figure 2.14: Cortical (yellow) and trabecular elements (white)

rial properties of ϵ_0=15GPa and ν=0.3 were set for both cortical and trabecular elements. These material properties correspond, at least for trabecular bone, to experimental results from nano-indentations [31]. The goal of the present study was to determine the reproducibility of the analysis. The exact setting of the material properties was not thought to have a major impact on the reproducibility. ϵ_0 of the cortical elements could have also been set to values, reported for cortical bone (e.g. [23]).

Boundary conditions were set to simulate a high friction uni-axial compression test: all nodes on the proximal boundary plane were fully constrained, all nodes at the distal boundary plane were displaced 0.1mm in proximal (=u_3) direction,

the other two DOFs of these nodes were constrained (see Fig. 2.15).

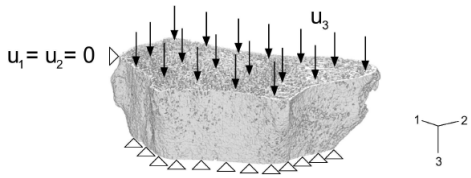

Figure 2.15: Boundary conditions for the uni-axial compression test for a typical MD region; from [36]

Due to the model sizes of typically ∼2 million elements and the number of analyses which were performed, the analysis was restricted to a linear analysis, using the special purpose solver, parFE [4]. parFE is a scalable parallel Finite Element solver, developed for the μFE analysis of bone models.

All μFE calculations were performed on a computer with 2x2 Xeon5160 CPUs (3GHz) and 64GB RAM. The number of elements was 1.8 million, 2.2 million and 3.0 million for STD, MD and DS regions, respectively. Mean CPU time was 34min, 43min and 57min for STD, MD and DS regions.

From the FE-output the resulting reaction forces on the restricted boundary plane were summed up. The apparent stiffness $K^{\mu FE}$ [kN/mm] was calculated by dividing the total reaction force with the applied displacement of 0.1mm. The ultimate force $F_{ult}^{\mu FE}$ [kN], representing failure, could not be directly determined from a linear analysis. An effective tissue strain based criterion, developed by Pistoia et.al. [27], was used. Here the force, to strain 2% of all elements beyond 0.7%, is determined. The ultimate force was computed by the aid of a failure safety factor, relating this ultimate force to the resulting total reaction force, resulting from the linear analysis.

Additionally, the apparent strength $\sigma_Y^{\mu FE}$ [MPa] and the overall apparent modulus $E_{app}^{\mu FE}$ [MPa] were determined. These values were calculated with the average cross sectional area A_{avg} [mm^2] (Eq. 2.3) and the length of the region h [mm]:

$$A_{avg} = V_{BONE}/h \tag{2.3}$$

$$\sigma_Y^{\mu FE} = F_{ult^{\mu FE}}/A_{avg} \tag{2.4}$$

$$E_{app}^{\mu FE} = \frac{K^{\mu FE} * h}{A_{avg}} \tag{2.5}$$

It has to be noted that $\sigma_Y^{\mu FE}$ represents an average stress within the model, under $F_{ult}^{\mu FE}$ applied. The actual stresses in elements, strained to 0.7%, can be up to one order of magnitude higher.

2.5 Homogenized FE Modelling and Analysis

2.5.1 Image Processing to create the hFE Models

All image processing procedures for generating the input mesh for homogenized FE analysis of the radius regions followed the developed framework described by Pahr & Zysset [26], and were fully implemented in `MedTool`.

Creation of a 1st rough 2D Surface Mesh

First a triangulated mesh of the circumferential boundary surface between trabecular and cortical bone (interface surface) was created, using Isosurf [34]. The binary 'inner' mask images were the basis of the triangulation and these were separated slice by slice into binary cross-sections. From these slices the first and last slice and, depending on the sampling resolution, 1 or 2 more slices in between were used as basis of the triangulation. The resulting triangulated surface included the distal and proximal boundary surface and the circumferential interface surface of the radius regions. The circumferential surfaces had two (STD and MD) or three (DS) triangles in height. These triangles were converted into a finite element mesh consisting of linear triangular elements.

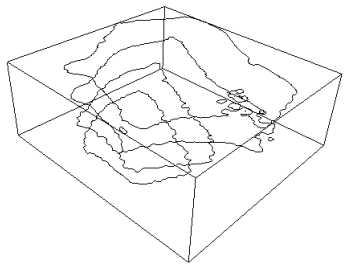

Figure 2.16: Contours used for the triangulation of a DS Region; the most distal contour is not one single closed line

Unfortunately these meshes were not appropriate for all samples. The sampled contours from the 'inner' masks were not all single closed contours, but contained artefacts, especially just beneath the lunate fossa, i.e. at the interface between

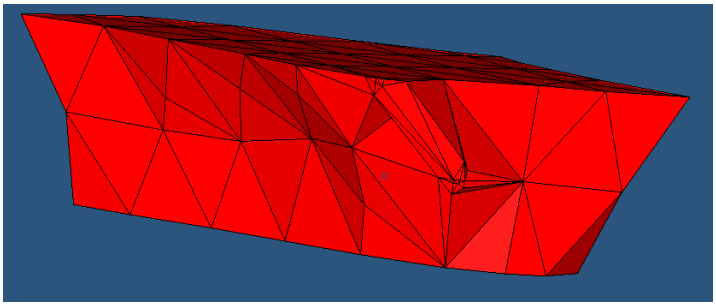

Figure 2.17: Severe problems with triangulation for a triangulated MD region

trabecular and cortical bone (see Fig. 2.16). This lead to problems with the triangulation. A severe case is shown on Figure 2.17. These problems were more present distally within the MD and DS regions, especially at the location of the distal radio-ulnar joint, and rarely happened at the STD regions.

Another problem arose from the varying region heights of the DS regions. As mentioned above three triangles in height should be created. The number of slices for the STD and MD Regions could be divided by two without residuals to 55 slices. This was the sampling resolution, and in order to have the last sampling slice still included in the image, the images had to be extended by one slice. These extensions were performed by copying the last slice. The effect on the overall volume fraction or fabric tensor was negligible. The height of the DS Regions could not always be divided by three without residuals. If that was the case, the sampling resolution was rounded to an integer, ranging from 48 to 62 slices. The voxel file of the 'inner' mask had to be extended or cropped to three times the sampling resolution plus 1 slice, because the the fourth sampled contour again had to remain inside the image. Thus the extension of the 'inner' masks accounted only for one or two slices.

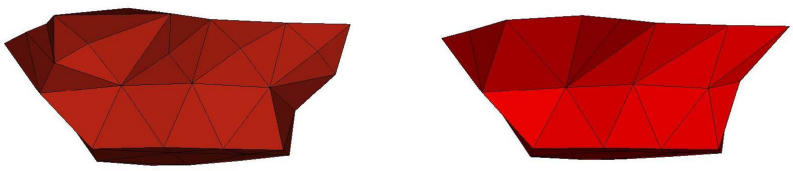

Figure 2.18: Initial triangular mesh (left) and the corresponding corrected mesh (right) of a STD region

Most of the MD and DS meshes and also some of the STD meshes had to be

corrected manually with a FE-Preprocessor (HyperMesh©, Altair Inc.), see Fig. 2.18. Care had to be taken not to have any holes in the mesh and all element normals always had to point outside.

Meshing the Bone Regions

With the triangulated 2D-surface mesh of the inner cortex contour and the 'thickness' mask of the corresponding region a volumetric mesh of the trabecular and the cortical bone was created. The trabecular regions were meshed with linear tetrahedral elements, using GMSH [13]. Additional nodes were created on averaged element normals, pointing towards outside the initial nodes on the circumferential mesh. The distance between these nodes and the nodes from the initial mesh was the cortical thickness from the corresponding 'thickness' masks. These nodes represent the outer cortical surface. HR-pQCT images were found to underestimate the cortical thickness by 20 % so the cortical thickness was corrected [36]. Additionally a minimum and maximum cortical thickness of 0.01mm and 3mm were defined to ensure cortical connectivity. Pentahedral elements ('wedge' elements) were created from the corresponding triangles from the inner and outer cortical surfaces, being the cortical 3D mesh. This initial mesh was refined two times, and finally the order of both trabecular (tetrahedrons) and cortical (pentahedrons) was changed from linear to quadratic elements. The resulting 3D-Mesh consisted of two element sets, cortical elements and trabecular elements. Additionally two node sets were defined, containing the nodes in the distal boundary plane and the proximal boundary plane, respectively. These node sets were used to apply the boundary conditions in the following.

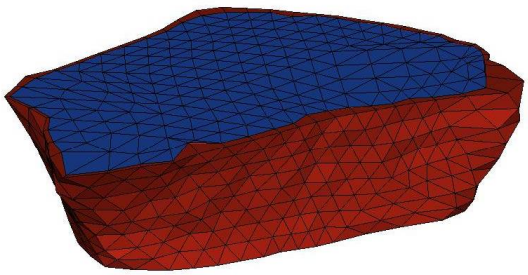

Figure 2.19: The resulting 3D mesh with trabecular (blue) and cortical (red) elements

The 'thickness' mask, containing the information about the cortical thickness,

had to have exactly the same dimension in height as the triangulated iso-surface for the recognition of the nodes of the top/bottom plane. Therefore also the 'thickness' masks of the DS Regions were also extended, by copying the last slice, or cropped to the right dimensions.

Mapping of the Trabecular and Cortical Architecture

The homogenized finite element analysis uses a description of the material properties of trabecular bone, following a morphology-elasticity based constitutive law, developed by Zysset & Curnier [40]. The 4th order compliance tensor $\mathbb{E}$ is defined according to Equation 2.6:

$$\mathbb{E} = \frac{1}{\rho^k} \begin{bmatrix} \frac{1}{\epsilon_0 m_1^{2l}} & \frac{-\nu_0}{\epsilon_0 m_1^l m_2^l} & \frac{-\nu_0}{\epsilon_0 m_1^l m_3^l} & 0 & 0 & 0 \\ \frac{-\nu_0}{\epsilon_0 m_2^l m_1^l} & \frac{1}{\epsilon_0 m_2^{2l}} & \frac{-\nu_0}{\epsilon_0 m_2^l m_3^l} & 0 & 0 & 0 \\ \frac{-\nu_0}{\epsilon_0 m_3^l m_1^l} & \frac{-\nu_0}{\epsilon_0 m_3^l m_2^l} & \frac{1}{\epsilon_0 m_3^{2l}} & 0 & 0 & 0 \\ 0 & 0 & 0 & \frac{1}{2G_0 m_2^l m_3^l} & 0 & 0 \\ 0 & 0 & 0 & 0 & \frac{1}{2G_0 m_3^l m_1^l} & 0 \\ 0 & 0 & 0 & 0 & 0 & \frac{1}{2G_0 m_1^l m_2^l} \end{bmatrix} \tag{2.6}$$

Here ϵ_0, G_0 and ν_0 are the Young's modulus, shear modulus and the Poisson's ratio of the isotropic pore-less material, respectively; m_i are the eigenvalues of the 2nd order fabric tensor $\mathbf{M}$; ρ is the volume fraction. k and l are the power coefficients for the density and the fabric eigenvalues, respectively.

This description requires the determination of the 2nd order fabric tensor $\mathbf{M}$ and the volume fraction ρ (BV/TV) for each element within the trabecular bone region. The mapping of the trabecular architecture follows the framework described by Pahr [26]. An isotropic 3D grid is laid over the HR-pQCT images of the STD, MD or DS regions. At every grid-point a sampling sphere is cropped, where the BV/TV and the 2nd order fabric tensor $\mathbf{M}$ are evaluated. BV/TV was evaluated from the BMD-scaled images and $\mathbf{M}$ from the corresponding segmented images. The grid distance was set to 3.0mm and the diameter of the sampling sphere was 7.5mm. The resulting fabric tensor $\mathbf{M}$ and the BV/TV were assigned to the tetrahedral elements of the finite element mesh of the trabecular bone region element by element via spatial interpolation (see Fig. 2.21). This procedure is fully automated and implemented in `MedTool`.

The evaluation of the 2nd order fabric tensor $\mathbf{M}$ was determined using the

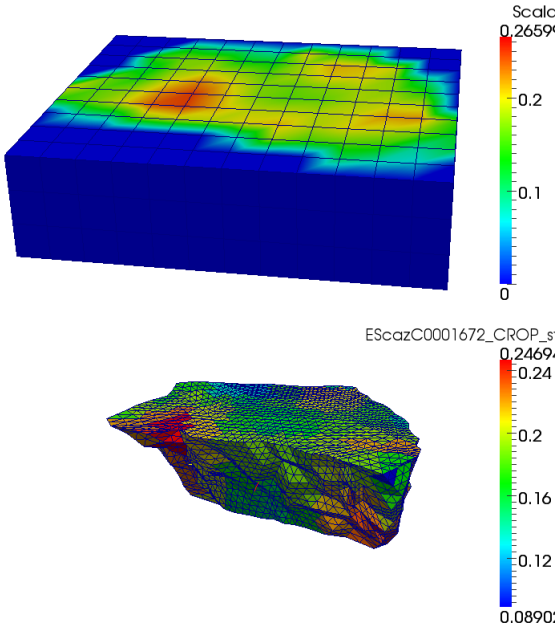

Figure 2.20: Volume fraction distribution of the whole grid (left) and assignment of these quantities to the elements of the trabecular compartment (right)

MIL-concept [38], which provides an orientation distribution function (ODF). This ODF is represented by a 2nd order tensor - the fabric tensor $\mathbf{M}$ (Eq. 2.7).

$$\mathbf{M} = \sum_{i=1}^{3} m_i \mathbf{m_i} \otimes \mathbf{m_i} \tag{2.7}$$

with $\mathbf{m_i}$ as the eigenvectors defining the main orientations ($i = 1, 2, 3$) and m_i are the corresponding eigenvalues ($m_1 < m_2 < m_3$). These eigenvalues were normalized such that the trace of $\mathbf{M}$ equals 3. The fabric tensor was evaluated from a segmented image. These segmented HR-pQCT images do, due to their insufficient resolution, not represent the trabecular architecture in detail. The orientation, i.e. the direction of the eigenvectors and the value of the eigenvalues, has to be corrected. The errors of the orientation of the fabric eigenvectors were relatively small, e.g. 5° for m_3 [36]. For the correction of the fabric eigenvalues, a calibration law was found, which relates the eigenvectors from segmented HR-pQCT images to those, evaluated from μCT images [36]:

$$m_{i,corr} = 1.7488 * m_{i,init} - 0.7488 \tag{2.8}$$

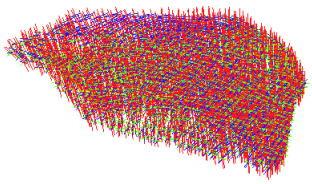

Figure 2.21: Fabric orientation of each trabecular element (right): red is major direction

The correction of the eigenvalues led to numerical problems in some trials and was neglected in the following studies. Also the correction of the fabric orientation was neglected. The BMD-scaled image has to be masked in order to evaluate the BV/TV only from the trabecular bone structure. A threshold must be set, above which the voxels are taken into account for the BV/TV evaluation. BV/TV of a bony structure, evaluated from a segmented μCT image with spatial resolutions of e.g. 18μm (μCT20, Scanco Medical), gives the best representation of the BV/TV of trabecular bone. Density based BV/TV (BV/TV^{d}) is evaluated from HR-pQCT-images by calculating the vBMD and then dividing it through the density of fully mineralized bone tissue, reported to be 1200 mg/mm^3 [6]:

$$BV/TV^d = vBMD/1200 \tag{2.9}$$

HR-pQCT-based BV/TV^{d} was found to underestimate the BV/TV from μCT [36]. A calibration law was developed relating the density based vBMD to BV/TV:

$$BV/TV = (vBMD * 0.093103 + 3.51483)/100 \tag{2.10}$$

The same constitutive law, used for the trabecular elements (Eq. 2.6) had to be used for the cortical elements as well in the non-linear analysis. The evaluation of volume fraction and fabric orientation was also mandatory for the cortical region. The difference for the cortical elements was, that uniform material properties were defined for all elements. BV/TV and the eigenvalues of the 2nd order fabric tensor **M** were kept constant for all elements [23]. Only the fabric orientation, i.e. the eigenvectors of **M**, were adjusted to fulfil the orthotropy, observed in cortical bone. The axes of orthotropy were defined by the z-direction of the radius section (distal-

proximal-direction), being projected into the mid-plane of the wedge element (3), the normal of this mid-plane, being the radial direction (2) and the direction of the cross product of these two vectors, being the circumferential direction (1), see Figure 2.22. In order to meet experimental determined material properties, found for cortical bone, BV/TV was set to 0.883 and the fabric eigenvalues were set to: m_1=m_2=0.958, m_3=1.085 [23].

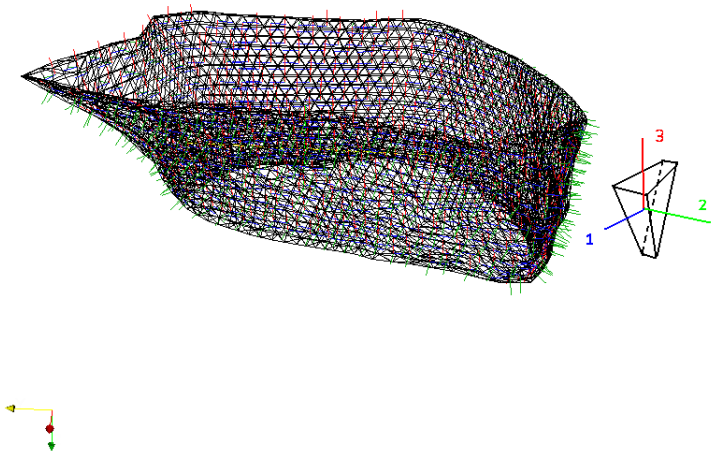

Figure 2.22: Wire frames of the cortex-elements with the corresponding material coordinate systems of each element

Calibration laws

The effect of the eigenvalue correction was investigated to some extent by recreating the STD baseline hFE models of six specimens (three pairs), covering the range of the obtained results, with a modified eigenvalue calibration law:

$$m_{i,corr} = 1.5 * m_{i,init} - 0.5 \tag{2.11}$$

It has also to be noted that the BV/TV calibration law was developed for distal radius sections, which were dissected free from all soft tissue and scanned in water-filled cylinders. It needed to be investigated, whether this calibration law would lead to reasonable results also for the scanning procedure in this study (whole forearm with soft tissue, no water-filled cylinder). The same six models,

used to check the eigenvalue correction, were again recreated with a calibration law for BV/TV, developed for scans of the whole forearm *in vitro* (unpublished data from Varga P.):

$$BV/TV = (vBMD * 0.088623 + 4.6334)/100 \tag{2.12}$$

2.5.2 hFE Analysis

The constitutive law for elasticity from Zysset and Curnier [40], described above (Eq. 2.6), was extended for damage and yield behaviour by Garcia [12]. A plastic yield function Y^P and a damage threshold function Y^D were defined, according to Eq. 2.13 & 2.5.2:

$$Y^P = \sqrt{\mathbf{S}^P : \mathbb{E}\mathbf{S}^P} - \sigma^P(D) \tag{2.13}$$

with $\mathbf{S}^P$ as the plastic part of the second Piola-Kirchhoff stress tensor and $\sigma^P(D)$ as the hardening function, according to Eq. 2.14.

$$\sigma^P(D) = \chi_p(1 - e^{-wD}) \tag{2.14}$$

D is the damage parameter ranging from intact ($D = 0$) to totally damaged ($D = 1$), and

$$Y^D = \begin{cases} \sqrt{\mathbf{S}^D : \mathbb{F}^+\mathbf{S}^D} - r^D(D) \leq 0 & \text{if } m(\mathbf{S}^D) \geq 0 \\ \sqrt{\mathbf{S}^D : \mathbb{F}^-\mathbf{S}^D} - r^D(D) \leq 0 & \text{if } m(\mathbf{S}^D) < 0 \end{cases}$$

here, $\mathbf{S}^D$ is the damage stress tensor, $r^D(D)$ defines the evolution of the damage (Eq. 2.15).

$$r^D(D) = R(1 + \chi_D(1 - e^{-vD}) \tag{2.15}$$

The fourth rank strength tensors $\mathbb{F}^{\pm}$ include the volume fraction (BV/TV) and the fabric ($\mathbf{M}$) as well as the material parameters for the idealized poreless material. For further and more detailed descriptions of this constitutive relationship, see Garcia et.al. [12]. The extrapolated properties of the poreless tissue were the same for trabecular and cortical bone. The elastic parameters were taken from [36]:

$$\begin{aligned} &\epsilon_0 = 15GPa, \quad \nu_0 = 0.227 \\ &k = 1.745 \qquad\quad l = 1.333 \end{aligned} \tag{2.16}$$

The plastic and damage parameters were adjusted to meet the yield and damage surfaces, reported by Rincon et.al. [31], with the elastic parameters:

$$\begin{aligned} &\sigma_0^+ = 96.0MPa, \quad \chi_0^+ = -0.263 \\ &\sigma_0^- = 128.0MPa \quad \chi_0^- = 0.310 \\ &\tau_0 = 56.3MPa \\ &p = 1.745 \qquad\qquad q = 0.632 \end{aligned} \tag{2.17}$$

The whole constitutive law was provided in the form of an ABAQUS© user defined material (UMAT).

All hFE calculations were performed on a computer with 2x2.67GHz and 4GB RAM. The number of elements was 5100, 7000 and 8900 for STD, MD and DS regions, respectively. Mean CPU time was 33min, 45min and 90min for STD, MD and DS regions.

The ultimate force from the non-linear hFE analysis F_{ult}^{hFE} was defined as the maximum of the reaction force, observed during the analysis. The stiffness K^{hFE} was defined as the initial slope in the resulting force-displacement-curve. The apparent strength σ_Y^{hFE} and the overall apparent modulus E_{app}^{hFE} were calculated similar to the μFE derived strengths and moduli:

$$\sigma_Y^{hFE} = F_{ult}^{hFE}/A_{avg} \tag{2.18}$$

$$E_{app}^{hFE} = \frac{K^{hFE} * h}{A_{avg}} \tag{2.19}$$

2.6 Bone Densitometric Measurements

2.6.1 Bone Mineral Content (BMC)

The BMC was calculated from BMD-scaled images of the STD, MD and DS regions, which were masked with their corresponding 'outer' masks to exclude grey-scales from the surrounding soft tissue from the BMD evaluation, respectively. The sum of all voxel-values (*GreySum*) of these BMD-scaled images was calculated and multiplied with the voxel volume of $0.0082^3 cm^3$ = 5.51368E^{-7} cm^3.

$$BMC = GreySum(BMDscaled) * 0.0082^3 \tag{2.20}$$

2.6.2 Areal Bone Mineral Density (aBMD)

To simulate the aBMD measurement by DXA the volumetric image were projected along the dorsal-palmar direction. BMC was divided with the dorsal-palmar projected area A_{Proj} of the STD, MD and DS regions, respectively.

$$aBMD = BMC/A_{Proj} \tag{2.21}$$

To calculate these projected areas, the 'outer' masks were projected. In order to project all images along the dorsal-palmar axis within the images, these had to be rotated such, that the x-axis within the image became identical to the dorsal-palmar direction. During this rotation each image had to be re-sampled to the voxel grid, using linear interpolation. This procedure is at risk to induce partial-volume effects. The rotated 'outer' masks were projected such, that each pixel-value of the projected image was the sum of up all binary data along the projection axis. After that all non-zero values were set to 1. The sum of all pixel-data, multiplied by the pixel area, was then taken as the projected area of the STD, MD and DS Regions.

2.6.3 Volumetric Bone Mineral Density (vBMD)

vBMD for the STD, MD and DS Regions could be calculated from the BMC by dividing it with the bone volume, i.e. the volume within the outer cortical contour, from each corresponding region. This bone volume was the GreySum of the 'outer' masks, multiplied with the voxel volume. The volume could be cancelled out and vBMD was calculated from Eq. 2.22.

$$vBMD = GreySum(BMDscaled)/GreySum('outer'mask) \tag{2.22}$$

2.7 Image Registration

The first series of scans was selected as the Baseline (BL) and the following five series were chosen as Follow Up (FU). To evaluate the effect of the repositioning error during reproducibility, i.e. compare results of unregistered FU scans to

those from registered FU scans, images of the identical bone regions from the BL scan and all FU scans had to be provided. There are several possibilities for image registration reported in literature: a 2D area matching method is provided by the manufacturer of the XtremeCT, using the large gradient of the cross-sectional area of the distal radius at its metaphysis [20]. 3D methods use 3D spatial rigid registration methods. Other studies showed common regions <100%, due to the fact that the original (BL) image and the image to be registered (FU), had the same dimensions, e.g. [22], [25]. In this study it was possible to get 100% common region, because the FU images had 330 slices, i.e. 27mm height. All FU images were registered to the corresponding BL images. If the repeated analysis is performed *in vivo*, it is better to change to a 'daisy-chain' method, i.e. register 1st FU to BL, register 2nd FU to 1st FU and so on. This procedure helps to overcome problems with finding corresponding trabecular structural patterns after a longer period of time, because bone remodelling substantially changed the trabecular architecture.

For the image registration, the above mentioned 3D spatial rigid registration methods from the C++ library ITK framework (Kiteware Inc., USA) was used. In principle the image registration tool does the following: It tries to find the corresponding images of the regions by: fixing the reference image, i.e. the Baseline, which should be found in the Follow Up images. Then the FU image is moved across the fixed image, using three translations and three rotations, i.e. six DOF. The cost function, a Mean Squares Metric (MS), is calculated at every step of the iteration (see Eq. 2.23). A minimum of MS is sought in a six dimensional space. The iteration is driven by a regular step gradient descent optimizer.

$$MS(BL, FU) = \frac{1}{N_{tot}} \sum_{i=0}^{N_{tot}} (BL_i - FU_i)^2 \tag{2.23}$$

BL_i and FU_i are the values of the corresponding voxels in the baseline and follow up images, N_{tot} is the total number of voxels. A break-criterion was set, allowing a maximum number of 150 iterations. If the break-criterion is met the registration stops and uses the resulting transformation of the last step. To reduce the computation time the large FU images of the STD and MD Regions (330 slices) were pre-cropped to 200 slices. The DS images were not pre-cropped.

The grey values of the surrounding soft tissue did not have a very high variation, but as the GOBJs were not identical. The registration would not only have to match the cortical and trabecular and cortical bone regions, but also the zeros

and non-zeros at the boundaries of the GOBJs.

To overcome these problems, the procedure set up in the following way: the raw STD, MD or DS baseline images as well as the pre-cropped raw STD, MD or DS follow up images were both masked with their corresponding 'outer' masks during the registration only, to identify the transformation of the follow up images. This transformation was applied to the unmasked follow up STD, MD or DS images and then the regions were cropped from this transformed unmasked follow up images, in order not to loose any cortical bone compartments on the follow up image.

For the DS Regions the image registration did not only find the corresponding region within the FU image. Also the image height, i.e. the number if image slices, which was varying for each specimen in the unregistered FU, was equal to the BL height for the corresponding registered FU.

A relation between the final MS and the variation of the results of the registered Follow Ups was investigated. As it can be seen from Equation 2.23, the mean was built up by a division through the whole number of voxels within the image. However all voxels outside the outer mask were set to 0 and are therefore not considered in the registration. So a convicted 'mean'-value, related to the voxels inside the outer mask was calculated:

$$MS_{BONE} = MS \frac{N_{tot}}{N_{BONE}} \tag{2.24}$$

This MS_{BONE} was related to the variation of all results to see, whether a good image registration, i.e. low MS_{BONE}, leads to a low variation of the Registered Follow Up results.

The image registration was, besides the Laplace-Hamming filtering, the most expensive process, in terms of computation. The registration was performed on a computer with 2x2.67GHz CPU and 4GB RAM and took 52min, 42 min and 41 min mean time for the STD, MD and DS regions.

All procedures, described before, i.e. from the BMD-scaling (Section 2.3.2) to the determination of the bone mineral densities (Section 2.6.1) were repeated one to one for all three regions, with one exception: the hFE analysis of the registered follow up of the DS regions was, like the analysis of the unregistered FU DS regions, not included in the present study.

Still, slight modifications were applied to the procedures, mostly to save computational time. The effect of varying iso-surfaces for individual specimens throughout the FU analyses was ruled out by taking the BL iso-surface for all FU

analyses of the individual specimens.

Now the results from the unregistered FU could be compared to those calculated from the registered FU to see, whether the extra effort for the image registration was justified, i.e. if the reproducibility improved.

2.8 Statistics

The baseline results could provide an overview of the properties of the set of specimens. These values could also be compared to results, reported in literature, to check whether all used procedures work properly.

Means and standard deviations (SD) of all measures were calculated as well as coefficients of variation (%CV), according to Equation 2.25, with X_j and SD_j as the mean and standard deviation of the FU from the specimen j.

$$\%CV_j = \frac{SD_j}{\overline{X_j}} \tag{2.25}$$

The correlations between μFE and hFE values were expressed with Pearson's correlation coefficients and Concordance correlation coefficients, according to Eq. 2.26, with $\sigma^{\mu FE}$ and σ^{hFE} as SD and $\overline{X}^{\mu FE}$ and $\overline{X}^{hFE}$ as means of the corresponding μFE and hFE results.

$$CC = \frac{2 * R^2 * \sigma^{\mu FE} * \sigma^{hFE}}{(\sigma^{\mu FE})^2 + (\sigma^{hFE})^2 + (\overline{X}^{\mu FE} - \overline{X}^{hFE})^2} \tag{2.26}$$

Precision errors were computed for the SD and %CV, being equal to root mean squared coefficient of variation, of the 60 ($\Rightarrow$ m=12 specimens $\times$ n=5 follow ups) measurements, following Equations 2.27 & 2.28.

$$PE_{SD} = \sqrt{\sum_{j=1}^{m} SD_j^2/m} \tag{2.27}$$

$$PE_{\%CV} = \sqrt{\sum_{j=1}^{m} \%CV_j^2/m} \tag{2.28}$$

95% confidence intervals for $PE_{\%CV}$ was calculated following Eq. 2.29 [19]:

$$\frac{m * (n-1)}{\chi^2_{0.025,m(n-1)}} PE^2_{\%CV} < \sigma^2 < PE^2_{\%CV} \frac{m * (n-1)}{\chi^2_{0.975,m(n-1)}} \tag{2.29}$$

with σ^2 as the true precision error of the coefficient of variation. The asymmetric χ^2 distribution was chosen here because precision errors cannot become negative, but have no upper limit.

The least significant change (LSC), being a change in a property, which can be quantified as significant [9], [17], was calculated according to Eq. 2.30, based on the precision errors $PE_{\%CV}$:

$$LSC = u_{0.975}\sqrt{2}PE_{\%CV} = 2.77PE_{\%CV} \tag{2.30}$$

with $u_{0.975}$ as the 97.5% quantile of the normal distribution. LSC can be interpreted as a threshold, above which changes do not represent the measurement errors.

Differences of the means between unregistered and registered Follow Ups as well as the differences of the means between STD and MD Region, MD and DS Region and STD and DS Region were tested for significance with a 2-tailed paired t-test. Changes of the variance, or SD, are checked for significance with a one sided Chi-squared test.

A term classically used in reproducibility studies is the interclass correlation coefficient (ICC) [32]. ICC describes the ratio of the inter-subject or within-subject variance to the population or between-subject variance. It ranges from 0 to 1, where 1 represents perfect reproducibility. ICC for all results of all regions were calculated according to Equations 2.31 to 2.37 [16].

$$ICC = \frac{BSV}{BSV + WSV} \tag{2.31}$$

with BSV as the between-subject variance and WSV as within-subject variance. WSV is calculated according to Eq. 2.32, BSV is calculated according to Eq. 2.33.

$$WSV = \frac{1}{m}\sum_{j=1}^{m} SD_j^2 \tag{2.32}$$

$$BSV = BSV_0 - \frac{WSV}{n} \tag{2.33}$$

with

$$BSV_0 = \frac{\sum_{j=1}^{m}\left(\overline{X_j} - \overline{X}\right)^2}{m-1} \tag{2.34}$$

95% confidence intervals (L95...lower border; U95...upper border) for ICC were calculated according to Eq. 2.35 to 2.37.

$$L95 = \frac{F_0/F_{0.025,m-1,m(n-1)} - 1}{(m-1) + F_0/F_{0.025,m-1,m(n-1)}} \tag{2.35}$$

$$U95 = \frac{F_0/F_{0.975,m-1,m(n-1)} - 1}{(m-1) + F_0/F_{0.975,m-1,m(n-1)}} \tag{2.36}$$

with

$$F_0 = \frac{BSV_0}{WSV/n} \tag{2.37}$$

Chapter 3

Results

3.1 Baseline Results for all three Regions

The results from the STD regions were compared with the results of the MD and DS regions, to quantify the effects of the distal shift of the region and the region enlargement, respectively. The results of the μFE analysis were also compared to the results from the hFE analysis, to verify the performance of the hFE analysis for the three regions of the distal radius. The complete baseline results are shown on Table 3.1.

BMC increased slightly with the distal shift, from the STD to the MD region, and for the region extension towards the DS regions. vBMD and aBMD were found to be lower for the MD regions than for the STD regions. vBMD for the DS regions lay between the resulting values for standard and most distal regions, aBMD for the DS regions was higher than aBMD for both STD and MD regions.

The resulting μFE stiffnesses ($K^{\mu FE}$) for the MD regions were lower than those for the STD regions, but this decrease was not significant (p=0.055). $K^{\mu FE}$ for the the DS regions was found to be ∼35% lower than for the STD and MD regions, but stiffnesses were not comparable, due to the different region sizes. The resulting hFE stiffnesses (K^{hFE}) were similar to those from the μFE calculations, but the STD-MD difference (7.0%) was now found to be significant. K^{hFE} for the the DS regions was found to be ∼55% lower than for the STD and MD region, but these stiffnesses were again not comparable. The ultimate forces from the μFE analysis ($F_{ult}^{\mu FE}$) did not change, neither with the shift from the STD to the MD region nor with the region enlargement to the DS region. The hFE ultimate forces (F_{ult}^{hFE}) showed significant decreases from STD to MD regions and from MD to

Parameter	**STD** Region	**MD** Region	Diff. [%] STD-MD	**DS** Region	Diff. [%] STD-DS
A_{avg} [mm^2]	347±79	473±110	+36.5±7.2^{p}	420±104	+20.8±7.4^{p}
BMC [HA mg]	715.5±158.9	736.5±199.5	+2.2±9.9	1080.3±271.9	-
vBMD [HA mg/cm^3]	233.4±52.0	175.6±43.5	-25.0±7.7^{p}	198.0±49.7	-15.6±5.4^{p}
aBMD [HA g/cm^2]	0.298±0.059	0.268±0.063	-10.1±8.2^{p}	0.303±0.062	+1.8±8.2
$K^{\mu FE}$ [kN/mm]	85.03± 24.05	80.30±26.46	-6.3±8.8	(53.88±16.72)	-
$F_{ult}^{\mu FE}$ [kN]	3.97±1.11	3.90±1.21	-2.3±8.3	3.83±1.16	-4.0±6.0
$E_{app}^{\mu FE}$ [MPa]	2262±622	1557±447	-31.2±7.0^{p}	(1759±514)	-
$\sigma_Y^{\mu FE}$ [MPa]	11.7±3.0	8.4±2.2	-28.3±6.0^{p}	(9.3±2.4)	-
K^{hFE} [kN/mm]	83.83±17.85	78.75±22.33	-7.0±9.6^{p}	(37.49±9.24^{x})	-
F_{ult}^{hFE} [kN]	5.42±1.27^{x}	4.76±1.38^{x}	-13.0±9.4^{p}	3.02±0.83^{x}	-44.6±6.4^{p}
E_{app}^{hFE} [MPa]	2220±449	1533±401	-31.6±8.2^{p}	(1227±318^{x})	-
σ_Y^{hFE} [MPa]	15.9±3.5^{x}	10.3±2.7^{x}	-36.1±7.6^{p}	(7.4±2.2^{x})	-

Table 3.1: Baseline results for STD & MD: mean±SD; mean±SD of the differences between STD & MD; baseline results for DS; mean±SD of the differences between STD & DS; ^{p} differences between regions are significant; ^{x} differences between hFE and μFE are significant; - not comparable

DS regions.

The apparent moduli, derived from the μFE analysis ($E_{app}^{\mu FE}$) were higher for the STD than for the MD regions. $E_{app}^{\mu FE}$ for the DS regions lay between the values for STD and MD regions. The same results were observed for the apparent moduli, calculated from the hFE analysis (E_{app}^{hFE}) of the STD and MD regions, respectively. The apparent modulus for the DS regions was lower than for STD and MD regions. Strengths, calculated from μFE ($\sigma_Y^{\mu FE}$) significantly decreased with the distal shift, and for the region extension to the DS regions, $\sigma_Y^{\mu FE}$ lay inbetween the results for STD and MD regions. hFE strengths (σ_Y^{hFE}) also decreased with the distal shift and with the region extension.

The hFE stiffnesses (K^{hFE}) for the STD and MD regions were not found to differ from those, acquired by the μFE calculations. Pearson's correlations (R^2) as well as Concordance correlations (CC) were both high for the μFE-hFE comparison of stiffness (see Table 3.2). Also the apparent moduli of STD and MD regions from the hFE analysis (E_{app}^{hFE}) were not different to those from the μFE analysis, also meaning high R^2 and CC. hFE derived ultimate forces and strengths (F_{ult}^{hFE} & σ_Y^{hFE}) for both STD and MD regions were lower than the μFE derived values. For the DS regions all hFE results were significantly lower than the μFE results.

The correlation coefficients between bone mineral density results (BMC, vBMD & aBMD) and the FE-derived results (K, F_{ult}, E_{app} & σ_Y) are shown in Table

R^2	**STD**	**MD**	**DS**	CC	**STD**	**MD**	**DS**
K	0.968	0.972	0.931	K	0.924	0.956	0.454
F_{ult}	0.987	0.974	0.878	F_{ult}	0.566	0.790	0.630
E_{app}	0.966	0.955	0.929	E_{app}	0.914	0.948	0.469
σ_Y	0.983	0.960	0.868	σ_Y	0.518	0.718	0.649

Table 3.2: Pearson's correlation coefficients (R^2, left) and Concordance correlation coefficients (CC, right) of μFE and hFE comparison; STD standard region, MD most distal region, DS double section region

3.3. It can be seen that the correlations between *structural* measures, i.e. BMC-K and BMC-F_{ult}, were high for both μFE and hFE results (μFE: R^2 >0.90; hFE: R^2 >0.89). Correlation coefficients for the *material* measures, i.e. a,vBMD-E_{app} & a,vBMD-σ_Y, were also high for both μFE and hFE (above 0.90 and 0.86 for μFE and hFE, respectively). For aBMD, a distinction between correlation coefficients for *structural* (K & F_{ult}) or *material* (E_{app} & σ_Y) measures could not be shown.

Region	**STD**			**MD**			**DS**		
Param.	BMC	vBMD	aBMD	BMC	vBMD	aBMD	BMC	vBMD	aBMD
$K^{\mu FE}$	**0.925**	0.471	**0.814**	**0.949**	0.601	**0.882**	**0.909**	0.426	**0.807**
$F_{ult}^{\mu FE}$	**0.934**	0.405	0.782	**0.960**	0.552	**0.868**	**0.950**	0.409	**0.800**
$E_{app}^{\mu FE}$	0.449	**0.931**	**0.805**	0.613	**0.931**	**0.843**	0.509	**0.936**	0.670
$\sigma_Y^{\mu FE}$	0.488	**0.917**	**0.821**	0.626	**0.926**	**0.853**	0.560	**0.909**	0.694
K^{hFE}	**0.909**	0.574	0.683	**0.935**	0.574	**0.838**	**0.892**	0.349	0.773
F_{ult}^{hFE}	**0.964**	0.372	0.779	**0.957**	0.610	**0.874**	**0.898**	0.499	0.778
E_{app}^{hFE}	0.265	**0.866**	0.645	0.463	**0.875**	0.696	0.475	**0.913**	0.544
σ_Y^{hFE}	0.408	**0.953**	0.794	0.504	**0.924**	0.752	0.477	**0.894**	0.542

Table 3.3: Pearson's Correlation Coefficients R^2 of the comparison between bone mineral density and FE results, bold numbers indicate high correlations (R^2 >0.8)

Modified calibration laws

The usage of the modified fabric calibration law (Eq. 2.11) resulted in increased stiffnesses and ultimate forces for these six models of 9% to 22% and 3% to 8%, respectively. The BV/TV correction for whole arms led also to increased stiffnesses and ultimate forces (2% to 4% for both K^{hFE} and F_{ult}^{hFE}).

3.2 Resulting Reproducibility and Improvement through Image Registration

First the performance of the XtremeCT was checked by the aid of the BMC-results of the STD region. The normalized differences between baseline and follow up showed SDs below 1.5% (see Tab. 3.4). No systematic decrease or increase of the mineral content throughout the follow up scans could be determined.

STD Region - BMC : Baseline - unreg. Follow Up						
Specimen	$BL - FU_1$	$BL - FU_2$	$BL - FU_3$	$BL - FU_4$	$BL - FU_5$	Mean±SD
A_F_1914_R	-1.19	-0.23	-1.06	-1.17	2.04	-1.14±0.64
B_F_1914_L	1.60	0.33	2.24	1.41	0.81	1.28±0.74
C_M_1938_R	1.47	-2.36	-1.18	-0.58	-2.70	-1.07±1.66
D_M_1938_L	-0.44	1.01	0.56	0.65	-1.11	0.13±0.88
E_M_1941_R	1.25	-0.08	1.62	1.98	2.86	1.53±1.08
F_M_1941_L	1.44	1.74	0.84	1.57	1.38	1.39±0.34
G_F_1918_R	-0.20	-2.68	-0.50	-1.45	-1.39	-1.24±0.97
H_F_1918_L	-2.04	-0.79	-0.60	-3.05	0.36	-1.22±1.33
I_F_1930_R	-0.47	-0.99	0.55	-1.17	0.02	-0.41±0.71
J_F_1930_L	-0.39	-0.72	-0.52	-2.26	-3.02	-1.38±1.18
K_F_1951_R	0.28	0.69	0.30	0.20	0.72	0.44±0.25
L_F_1951_L	-0.36	0.74	1.34	0.25	-0.10	0.37±0.68
Mean±SD	0.08±1.16	-0.28±1.32	0.30±1.09	-0.30±1.58	-0.35±1.75	**-0.11±1.38**

Table 3.4: Differences between baseline and follow up for STD BMC in [%]); right: specimen mean±SD; bottom: measurement mean±SD; bold numbers on right bottom: overall mean±SD

The unregistered follow up results did not differ from the baseline results, i.e. the mean±SD of the normalized differences included 0. This could also be observed for the other BMD measures (vBMD & aBMD) and the μFE and hFE results. The overall mean±SD are summarized in the left column in Table 3.5. The image registration reduced the SD of the Δ(BL - reg. FU) of all measures and additionally induced a shift of the FE results: the μFE results decreased and the hFE results increased (see Tab. 3.5). The bone mineral density measures showed no such shift. These shifts and decreased SD can also be seen on Figures 3.1, 3.2 & 3.3.

The precision errors of the standard deviation (PE_{SD}) can express, to some extent, the reproducibility, but the precision error of the coefficients of variation ($PE_{\%CV}$) can give a better insight, these are normalized measures, i.e. the large between-subject-variance is eliminated.

$PE_{\%CV}$ of the bone mineral density measurements ranged from 1% to 2%,

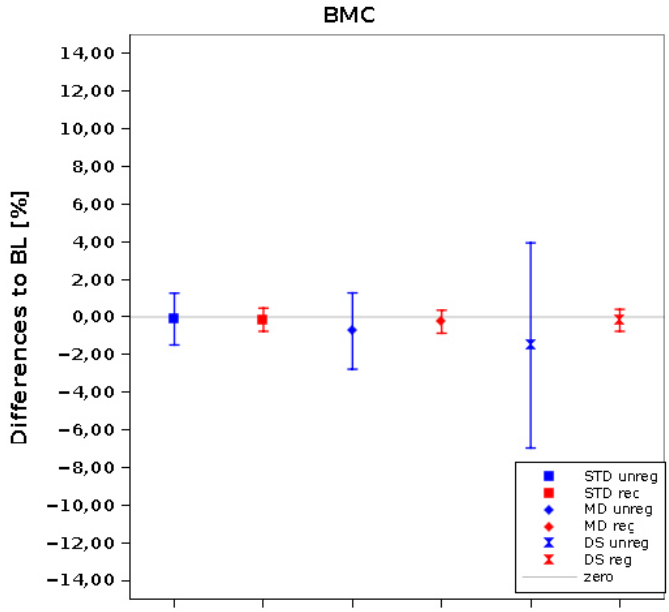

Figure 3.1: Mean±SD of the BMC differences [%] between BL and unregistered FU (blue) and registered FU (red) for STD (left), MD (middle) and DS regions (left)

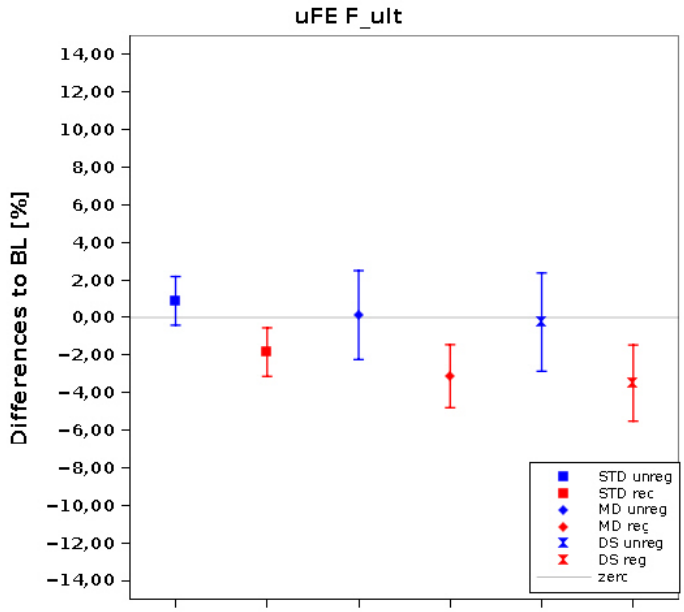

Figure 3.2: Mean±SD of the $F_{ult}^{\mu FE}$ differences [%] between BL and unregistered FU (blue) and registered FU (red) for STD (left), MD (middle) and DS regions (left)

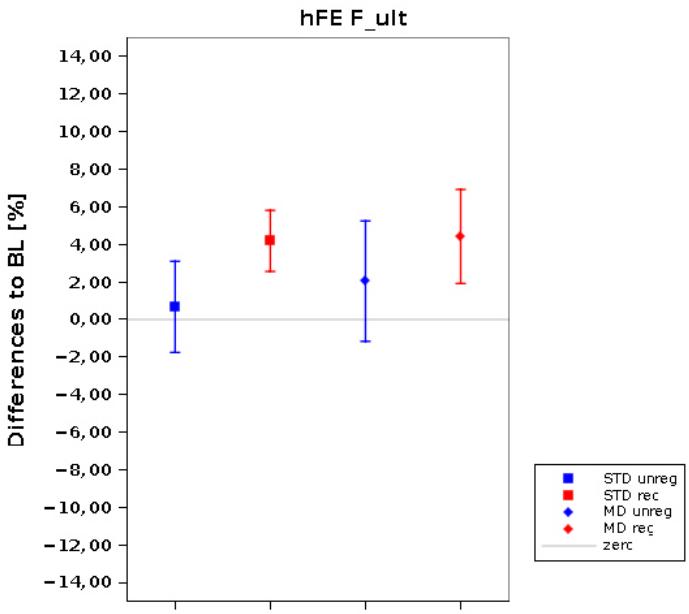

Figure 3.3: Mean±SD of the F_{ult}^{hFE} differences [%] between BL and unregistered FU (blue) and registered FU (red) for STD (left), MD (middle) and DS regions (left)

1.5% to 3% and 4% to 4.5% for the STD, MD and DS regions, respectively (see Tab. 3.6). $PE_{\%CV}$ of BMC and vBMD could be decreased by image registration for STD, MD and DS regions to <0.5%, <0.6% and <0.6%, respectively. aBMD showed the least decreases for the STD, MD and DS regions.

$PE_{\%CV}$ of the resulting stiffnesses $K^{\mu FE}$ & K^{hFE} and ultimate forces $F_{ult}^{\mu FE}$ & F_{ult}^{hFE} lay within 1.1% to 1.7%, 2.0% to 3.3% and 2.1% to 5.5% for STD, MD and DS regions, respectively (see Tab. 3.7). $PE_{\%CV}$ of the resulting apparent moduli $E_{app}^{\mu FE}$ & E_{app}^{hFE} and apparent strengths $\sigma_Y^{\mu FE}$ & σ_Y^{hFE} lay within 2.4% to 3.3%, 2.8% to 4.2% and 4.5% to 4.9% for STD, MD and DS regions, respectively (see Tab. 3.7).

Image registration was able to improve the reproducibility, i.e. decrease the precision errors. For the STD region the decrease of the precision errors was lowest, compared to the other regions. The precision errors of the μFE and hFE results could be decreased to 0.6% to 0.8%, 1.0% to 1.4 % (except K^{hFE} & E_{app}^{hFE}) and 1.1% to 1.4% for STD, MD and DS regions, respectively (see Tab. 3.7).

Least significant changes (LSC) showed decreases, identical to those of the $PE_{\%CV}$, through the image registration (see Tab. 3.8). These values represent the clinically relevant data, i.e. the threshold to pass to quantify a change as

significant.

The calculated ICCs showed a high reproducibility of all measures already for the unregistered STD and MD regions, ranging from 0.992 (vBMD) to 0.998 (BMC, μFE Stiffn., μFE F_{ult}) and 0.986 (hFE F_{ult}) to 0.997 (BMC), respectively. ICCs for the unregistered DS regions ranged from 0.965 (vBMD, μFE Stiffn.) 0.995 (μFE F_{ult}). The image registration further improved the reproducibility. ICCs for the registered STD, MD and DS region ranged now from 0.996 (aBMD) to 1.000 (BMC, vBMD, μFE F_{ult}), 0.993 (hFE Stiffn.) to 1.000 (BMC, vBMD) and 0.994 (aBMD) 1.000 (vBMD, BMC), respectively.

The decrease of the subject specific %CVs, i.e. %CV before image registration minus %CV after image registration, was related to the resulting MS_{BONE} from the image registration. The correlation coefficients were all low (<0.35) and no significant trend could be found (e.g. see Fig. 3.4).

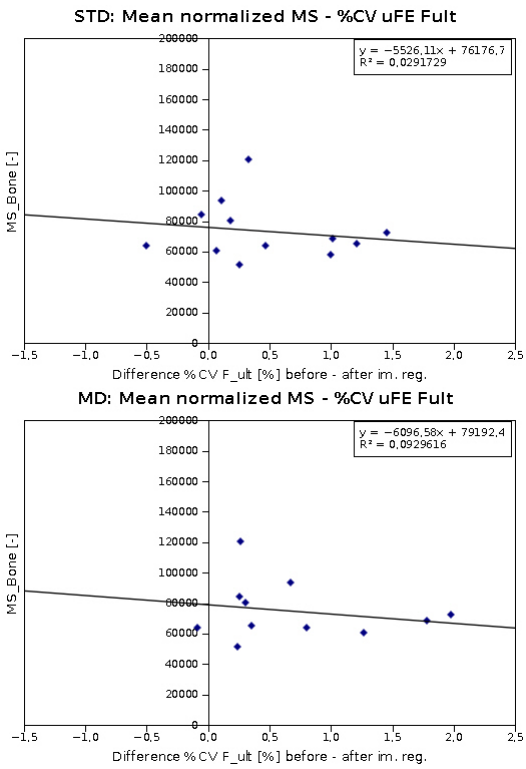

Figure 3.4: Comparison of the differences of %CV (μFE F_{ult}) before and after the image registration and MS_{BONE} STD regions (left) and MD regions (right)

STD Region			
Parameter	mean Δ BL - unreg. FU	mean Δ BL - reg. FU	mean Δ unreg. - reg. FU
A_{avg}	-0.2±2.2	0.0±0.1	-0.2±2.3
BMC	-0.1±1.4	-0.2±0.6	0.0±1.2
vBMD	-2.1±14.3	-1.0±2.7	0.3±2.4
aBMD	0.2±2.4	-0.1±0.6	-1.2±1.3
$K^{\mu FE}$	-0.9±1.4	-1.8±1.3	-2.7±2.1
$F_{ult}^{\mu FE}$	0.9±1.3	-1.8±1.3	-2.4±2.1
$E_{app}^{\mu FE}$	1.2±3.1	-1.8±1.4	-3.3±3.3
$\sigma_Y^{\mu FE}$	1.2±2.8	-1.8±1.3	-3.0±3.6
K^{hFE}	0.4±2.0	3.0±1.5	2.6±2.0
F_{ult}^{hFE}	0.7±2.4	4.2±1.6	3.5±2.5
E_{app}^{hFE}	0.7±2.4	4.2±1.6	3.5±2.5
σ_Y^{hFE}	0.7±2.4	4.2±1.6	3.5±2.5
MD Region			
Parameter	Δ BL - unreg. FU	Δ BL - reg. FU	Δ unreg. - reg. FU
A_{avg}	0.3±4.1	-0.1±0.3	-0.6±4.0
BMC	-0.7±2.0	-0.3±0.6	-0.5±1.9
vBMD	-3.6±16.5	-1.3±2.7	-0.8±3.7
aBMD	-0.9±3.6	-0.2±0.6	-1.8±1.3
$K^{\mu FE}$	0.1±2.8	-3.3±2.0	-3.5±3.0
$F_{ult}^{\mu FE}$	0.1±2.4	-3.1±1.7	-2.8±2.8
$E_{app}^{\mu FE}$	-0.1±4.5	-3.2±2.1	-2.7±4.5
$\sigma_Y^{\mu FE}$	-0.1±3.9	-3.0±1.8	-3.2±4.2
K^{hFE}	1.2±2.9	2.6±3.4	1.4±3.1
F_{ult}^{hFE}	2.0±3.2	4.4±2.5	2.4±3.1
E_{app}^{hFE}	1.1±4.8	2.7±3.2	1.8±5.0
σ_Y^{hFE}	1.9±4.9	4.5±2.3	2.8±5.0
DS Region			
Parameter	Δ BL - unreg. FU	Δ BL - reg. FU	Δ unreg. - reg. FU
A_{avg}	0.8±5.9	-0.1±0.2	0.9±5.9
BMC	-1.5±5.5	-0.2±0.6	-1.3±5.5
vBMD	-1.1±3.7	-0.1±3.9	-1.1±5.5
aBMD	2.1±9.8	0.9±3.8	0.4±4.3
$K^{\mu FE}$	-0.5±6.5	-3.6±2.2	-2.6±15.2
$F_{ult}^{\mu FE}$	-1.9±13.1	-3.5±2.0	-1.9±13.8
$E_{app}^{\mu FE}$	-2.7±14.3	-3.5±2.3	-0.2±14.6
$\sigma_Y^{\mu FE}$	-1.5±14.3	-3.4±2.1	-2.2±15.1

Table 3.5: Differences (in [%]) between BL and unregistered/registered FU and between unregistered and registered FU; hFE DS Follow Ups not calculated

STD	Unregistered FU		Registered FU		reduction
Param.	$PE_{\%CV}$	95%CI (Width)	$PE_{\%CV}$	95%CI (Width)	of $PE_{\%CV}$
BMC	0.959	0.800-1.198 (0.398)	0.437	0.364-0.545 (0.181)	54.5%*
vBMD	2.114	1.763-2.642 (0.878)	0.422	0.352-0.527 (0.175)	80.0%*
aBMD	1.509	1.258-1.885 (0.627)	1.413	1.178-1.765 (0.587)	6.4%
MD	Unregistered FU		Registered FU		reduction
Param.	$PE_{\%CV}$	95%CI (Width)	$PE_{\%CV}$	95%CI (Width)	of $PE_{\%CV}$
BMC	1.502	1.253-1.876 (0.624)	0.563	0.469-0.703 (0.234)	62.5%*
vBMD	3.079	2.568-3.846 (1.279)	0.544	0.453-0.679 (0.226)	82.3%*
aBMD	1.479	1.233-1.848 (0.614)	1.199	1.000-1.498 (0.4.498)	18.9%
DS	Unregistered FU		Registered FU		reduction
Param.	$PE_{\%CV}$	95%CI (Width)	$PE_{\%CV}$	95%CI (Width)	of $PE_{\%CV}$
BMC	4.539	3.786-5.671 (1.886)	0.510	0.425-0.637 (0.212)	88.8%*
vBMD	4.545	3.790-5.678 (1.888)	0.495	0.413-0.618 (0.206)	89.1%*
aBMD	4.069	3.394-4.084 (1.690)	1.656	1.381-2.069 (0.688)	59.3%*

Table 3.6: $PE_{\%CV}$ of the bone mineral density measures for unregistered/registered FU of the STD, MD and DS Regions; * 95%CI of unreg. and reg. FU do not overlap

STD	Unregistered FU		Registered FU		reduction of
Param.	$PE_{\%CV}$	95%CI (Width)	$PE_{\%CV}$	95%CI (Width)	$PE_{\%CV}$
$K^{\mu FE}$	1.327	1.107-1.658 (0.551)	0.782	0.652-0.977 (0.325)	41.0%*
$F_{ult}^{\mu FE}$	1.160	0.967-1.449 (0.482)	0.707	0.589-0.883 (0.293)	39.1%*
$E_{app}^{\mu FE}$	2.760	2.301-3.448 (1.146)	0.761	0.635-0.951 (0.316)	72.4%*
$\sigma_Y^{\mu FE}$	2.417	2.015-3.019 (1.004)	0.687	0.573-0.858 (0.285)	71.6%*
K^{hFE}	1.185	0.988-1.480 (0.492)	0.709	0.591-0.885 (0.294)	40.2%*
F_{ult}^{hFE}	1.702	1.420-2.127 (0.707)	0.790	0.659-0.987 (0.328)	53.6%*
E_{app}^{hFE}	2.509	2.092-3.135 (1.043)	0.688	0.574-0.860 (0.286)	72.6%*
σ_Y^{hFE}	3.318	2.767-4.145 (1.378)	0.731	0.609-0.913 (0.304)	78.0%*
MD	Unregistered FU		Registered FU		reduction of
Param.	$PE_{\%CV}$	95%CI (Width)	$PE_{\%CV}$	95%CI (Width)	$PE_{\%CV}$
$K^{\mu FE}$	2.273	1.896-2.840 (0.944)	1.476	1.231-1.844 (0.613)	35.1%*
$F_{ult}^{\mu FE}$	2.049	1.709-2.560 (0.851)	1.191	0.993-1.488 (0.495)	41.9%*
$E_{app}^{\mu FE}$	3.304	2.755-4.128 (1.372)	1.476	1.230-1.843 (0.613)	55.3%*
$\sigma_Y^{\mu FE}$	2.856	2.381-3.568 (1.186)	1.193	0.995-1.491 (0.496)	58.2%*
K^{hFE}	3.032	2.529-3.788 (1.259)	2.399	2.001-2.997 (0.996)	20.9%
F_{ult}^{hFE}	3.233	2.696-4.039 (1.343)	1.044	0.870-1.304 (0.433)	67.7%*
E_{app}^{hFE}	3.889	3.243-4.859 (1.615)	2.407	2.007-3.007 (1.000)	38.1%*
σ_Y^{hFE}	4.169	3.476-5.208 (1.732)	1.295	0.864-1.295 (0.431)	75.1%*
DS	Unregistered FU		Registered FU		reduction of
Param.	$PE_{\%CV}$	95%CI (Width)	$PE_{\%CV}$	95%CI (Width)	$PE_{\%CV}$
$K^{\mu FE}$	5.572	4.647-6.961 (2.314)	1.361	1.135-1.700 (0.565)	75.6%*
$F_{ult}^{\mu FE}$	2.137	1.782-2.670 (0.888)	1.212	1.010-1.514 (0.503)	43.3%*
$E_{app}^{\mu FE}$	4.926	4.108-6.155 (2.046)	1.350	1.126-1.686 (0.560)	72.6%*
$\sigma_Y^{\mu FE}$	4.497	3.750-5.618 (1.868)	1.208	1.007-1.509 (0.502)	73.1%*

Table 3.7: $PE_{\%CV}$ of the bone mineral density measures for unregistered/registered FU of the STD, MD and DS regions; hFE FU for DS not calculated; * 95%CI of unreg. and reg. FU do not overlap

STD Region		
Parameter	unreg. FU	reg. FU
BMC [mg HA]	19.0 (2.66)	8.7 (1.22)
vBMD [HA mg/cm^3]	13.7 (5.86)	3.5 (1.17)
aBMD [HA g/cm^2]	0.012 (4.18)	0.012 (3.91)
$K^{\mu FE}$ [kN/mm]	3.15 (3.68)	1.81 (2.17)
$F_{ult}^{\mu FE}$ [kN]	0.13 (3.21)	0.08 (1.96)
$E_{app}^{\mu FE}$ [MPa]	175 (7.64)	47 (2.11)
$\sigma_Y^{\mu FE}$ [MPa]	0.8 (6.70)	0.2 (1.90)
K^{hFE} [kN/mm]	2.75 (3.28)	1.68 (1.96)
F_{ult}^{hFE} [kN]	0.3 (4.72)	0.1 (2.19)
E_{app}^{hFE} [MPa]	156 (6.95)	44 (1.91)
σ_Y^{hFE} [MPa]	1.48 (9.19)	0.3 (2.02)
MD Region		
Parameter	unreg. FU	reg. FU
BMC [mg HA]	30.4 (4.16)	11.4 (1.55)
vBMD [HA mg/cm^3]	14.8 (8.53)	2.6 (1.51)
aBMD [HA g/cm^2]	0.011 (4.10)	0.009 (3.32)
$K^{\mu FE}$ [kN/mm]	5.05 (6.30)	3.18 (4.09)
$F_{ult}^{\mu FE}$ [kN]	0.22 (5.68)	0.13 (3.33)
$E_{app}^{\mu FE}$ [MPa]	142 (9.15)	62 (4.09)
$\sigma_Y^{\mu FE}$ [MPa]	0.7 (7.91)	0.3 (3.31)
K^{hFE} [kN/mm]	6.69 (8.40)	5.37 (6.65)
F_{ult}^{hFE} [kN]	0.4 (8.96)	0.1 (2.89)
E_{app}^{hFE} [MPa]	166 (10.77)	105 (6.67)
σ_Y^{hFE} [MPa]	1.20 (11.55)	0.3 (2.87)
DS Region		
Parameter	unreg. FU	reg. FU
BMC [mg HA]	134.0 (12.57)	15.2 (1.41)
vBMD [HA mg/cm^3]	24.5 (12.59)	2.7 (1.37)
aBMD [HA g/cm^2]	0.035 (11.27)	0.014 (4.59)
$K^{\mu FE}$ [kN/mm]	8.32 (15.43)	1.96 (3.77)
$F_{ult}^{\mu FE}$ [kN]	0.23 (5.92)	0.12 (3.36)
$E_{app}^{\mu FE}$ [MPa]	236 (13.65)	64 (3.74)
$\sigma_Y^{\mu FE}$ [MPa]	1.2 (12.46)	0.3 (3.35)

Table 3.8: LSC of bone mineral density and FE results for unregistered and registered STD, MD and DS regions: absolute values and percentage (in brackets); absolute values calculated with the mean of the unregistered or registered FU, respectively; hFE DS Follow Ups not calculated

STD	Unregistered FU		Registered FU	
Parameter	ICC	95% CI (Width)	ICC	95% CI (Width)
BMC	0.998	0.991-0.999 (0.008)	1.000	0.998-1.000 (0.002)
aBMD	0.995	0.975-0.996 (0.021)	0.996	0.977-0.997 (0.020)
vBMD	0.992	0.957-0.994 (0.037)	1.000	0.998-1.000 (0.002)*
$K^{\mu FE}$	0.998	0.990-0.999 (0.009)	0.999	0.997-1.000 (0.003)
$F_{ult}^{\mu FE}$	0.998	0.991-0.999 (0.008)	1.000	0.997-1.000 (0.003)
$E_{app}^{\mu FE}$	0.992	0.957-0.994 (0.037)	0.999	0.996-0.999 (0.003)*
$\sigma_Y^{\mu FE}$	0.992	0.960-0.994 (0.034)	0.999	0.995-0.999 (0.004*)
K^{hFE}	0.997	0.986-0.998 (0.012)	0.999	0.995-0.999 (0.005)
F_{ult}^{hFE}	0.996	0.978-0.997 (0.019)	1.000	1.000-1.000 (0.000)*
E_{app}^{hFE}	0.987	0.931-0.989 (0.058)	0.999	0.992-0.999 (0.007)*
σ_Y^{hFE}	0.982	0.910-0.986 (0.076)	0.999	0.993-0.999 (0.006)*
MD	Unregistered FU		Registered FU	
Parameter	ICC	95% CI (Width)	ICC	95% CI (Width)
BMC	0.997	0.983-0.998 (0.015)	1.000	0.998-1.000 (0.002)*
aBMD	0.996	0.981-0.997 (0.016)	0.998	0.988-0.998 (0.010)
vBMD	0.995	0.973-0.996 (0.023)	1.000	0.999-1.000 (0.001)*
$K^{\mu FE}$	0.995	0.975-0.996 (0.021)	0.998	0.990-0.999 (0.009)
F_{ult}^{hFE}	0.996	0.976-0.997 (0.021)	0.999	0.993-0.999 (0.006)
$E_{app}^{\mu FE}$	0.986	0.930-0.989 (0.060)	0.997	0.985-0.998 (0.013)
$\sigma_Y^{\mu FE}$	0.988	0.937-0.990 (0.054)	0.998	0.988-0.998 (0.010)
K^{hFE}	0.987	0.932-0.990 (0.058)	0.993	0.964-0.995 (0.031)
F_{ult}^{hFE}	0.986	0.929-0.989 (0.060)	0.999	0.993-0.999 (0.006)*
E_{app}^{hFE}	0.976	0.880-0.981 (0.101)	0.991	0.951-0.993 (0.042)
σ_Y^{hFE}	0.975	0.874-0.980 (0.106)	0.998	0.991-0.999 (0.008)*
DS	Unregistered FU		Registered FU	
Parameter	ICC	95% CI (Width)	ICC	95% CI (Width)
BMC	0.975	0.876-0.980 (0.104)	1.000	0.998-1.000 (0.002)*
aBMD	0.974	0.874-0.980 (0.106)	0.994	0.969-0.995 (0.026)
vBMD	0.965	0.831-0.972 (0.141)	1.000	0.998-1.000 (0.002)*
$K^{\mu FE}$	0.965	0.833-0.972 (0.139)	0.998	0.990-0.999 (0.009)*
F_{ult}^{hFE}	0.995	0.973-0.996 (0.023)	0.998	0.992-0.999 (0.007)
$E_{app}^{\mu FE}$	0.969	0.851-0.975 (0.124)	0.998	0.990-0.999 (0.009)*
$\sigma_Y^{\mu FE}$	0.971	0.858-0.977 (0.119)	0.998	0.989-0.998 (0.009*)

Table 3.9: ICCs and their 95% confidence intervals for all measured/calculated parameters of STD, MD and DS regions; hFE FU for DS not calculated; * 95%CI of unreg. and reg. FU do not overlap

Chapter 4

Discussion

In the following Chapter the obtained results and the limitations of this study are discussed. First the differences of the resulting values for all three analysed regions are discussed and the results are compared to results, found in literature. Then the reproducibility of the FE-results and the bone mineral density measurements is discussed as well as the effect of the image registration.

4.1 Resulting Baseline Values

The increased BMC of the MD region, compared to the STD region, resulted from the increased cross-sectional area of the radius with the distal shift, the MD region contained more bone volume. This increase was compensated by the lower bone mineral density (aBMD & vBMD) in the MD region. Therefore, and also because of the large between-subject-variance, the increase was not found to be significant. vBMD decreased more than aBMD. aBMD within this study was evaluated from projected HR-pQCT images. These values were found to correlate highly with clinical DXA measurements [10]. The images had to be rotated, in order to be able to project the images along the dorsal-palmar direction into the the radio-ulnar plane. The re-sampling after the image rotation included the risk to introduce partial volume effects to the rotated image. It remains unsure how these affect the aBMD, as there were no values determined for comparison. The $GreySum$ within the images was preserved throughout the rotation. All differences of bone mineral density between STD and MD region were found to be similar to those, previously reported by Varga et. al. [36].

BMC of DS region was not comparable to STD or MD regions, because BMC

is a *structural* value, i.e. it is dependent on dimensions of the considered region. BMC for DS regions was higher than BMC for STD or MD region. aBMD and vBMD could be compared as these were densities or *material* measures, i.e. independent of the region size. vBMD of the DS region lay in between the values of the STD and MD Region. The DS region is a combination of the STD ('more dense') and MD Region ('less dense'). The same was expected for aBMD, but not found in the results. aBMD for DS regions was slightly higher than aBMD of the STD and MD regions, but aBMD in this study was highly dependent on the projected areas of the distal radius regions.

The resulting stiffnesses and ultimate forces were also *structural* measures. Stiffnesses from STD and MD regions could be compared, because these were similar 9mm regions of the distal radius. When comparing the results of the linear μFE analysis to those from other studies, the material properties of the elements, i.e. homogeneous Young's Modulus, had to be considered. The material properties in this study were chosen to be equal for cortical and trabecular elements. This was not thought to have a major effect on the reproducibility in the following, but it still affects the absolute values of the μFE results. The μFE stiffnesses ($K^{\mu FE}$), obtained in this study, lay, with the issues mentioned above considered, in the same range as those, reported in literature, e.g. STD regions by Varga et.al. [36] (96.5±39.4kN), Boutroy et.al. [7] (124.7±25.9kN) or Vilayphiou et.al. [37] (112.1±27.5kN), MD regions by Varga et.al. [36] (84.6±44.8kN). Müller et.al. [24] reported lower stiffness for a smaller region (42.3kN with PE_{SD} 0.4kN), and when these results were scaled to the present Young's modulus, the stiffness was still below the results, obtained in this study. The μFE stiffness of the DS regions was, due to the different region dimension, not comparable to the STD or MD stiffness. Varga et.al. [36] reported a μFE stiffness of approximately 25kN/mm for 20mm regions of the distal radius. The DS regions in this study had heights of 13.25±0.41mm. The observed μFE stiffnesses of the DS regions lay in between the stiffnesses of the 9mm regions and those of the 20mm regions. The fact that the μFE stiffness of the MD regions were lower than the stiffness of the STD regions supports the suggestion, that the weakest region of the distal radius is rather included in the MD regions. The reason why this decrease was not found to be significant, like reported before [36], might have just been a result of the absolute properties of the provided set of forearms.

The ultimate forces, derived from the μFE analysis ($F_{ult}^{\mu FE}$), were slightly decreasing with the distal shift from STD to MD regions and for the region extension

to the DS region. These decreases were not significant. The resulting values were slightly below those, reported by Varga et.al. [36], although the modelling strategy was exactly the same. This might have been another effect of the properties of the provided set forearms. Recently, Boutroy et.al. [7] and Vilayphiou et.al. [37] reported also lower ultimate forces for the STD regions of 2.93±0.57kN and 2.65±0.67kN, respectively. In the current study, as well as in all mentioned references, the ultimate force from the linear μFE-analysis was determined using the Pistoia-criterion [27]. This criterion was developed for another resolution (165μm) and another region of the distal radius. It has been shown previously that the ultimate forces, determined with this criterion, still correlate highly with experimental ultimate forces at the present resolution and location [36]. Still, 2% of all elements in a model are not comparable for different model sizes. In models including the same structural pattern, e.g. the proximal part of the MD region was included in the STD region, and both STD and MD regions were included in the DS region, the elements, which are strained beyond the predefined yield-strain, could be found at the same location within the model. The models of the MD regions were larger than the models of the STD regions. The smaller model should reach the 2%-criterion earlier than the larger model, and should therefore have given a smaller ultimate force. The fact that the ultimate forces did not decrease with a region enlargement, leads to the conclusion that the highly strained elements were not localized in domains within the STD or MD regions. The correlation coefficients for the STD-DS or MD-DS comparison were higher for the MD region than for the STD region (MD-DS: R^2=0.986; STD-DS: R^2=0.956). The highly strained regions within the model, although not completely localized within the MD region, still are present within the MD region, which is also included in the DS region.

The apparent modulus from the μFE calculations ($E_{app}^{\mu FE}$) is, together with the apparent strength, a *material* measure, i.e independent of the model dimensions. It could therefore be compared between models of different dimensions. The term *material* refers to the material within the model, i.e. the cortical and trabecular bone structure within the radius regions. Like the μFE stiffness, also the apparent modulus decreased with the distal shift from STD to MD. This was another sign that the trabecular architecture in the MD region includes weaker parts of the distal radius than the STD region. The decrease of the stiffness was not found to be significant, but with the larger average cross-sectional area A_{avg} at the MD region the decrease of the apparent modulus was significant. The apparent

moduli for the DS region was also lower than for STD regions but higher than for the MD regions. This leads to the conclusion that the *material* within the STD region is stronger, compared to the *material* in the MD region, the DS region as a combination of these two, lay between them. The apparent modulus of the MD region showed again a slightly better correlation coefficient for the STD-DS or MD-DS comparison: R^2=0.956, compared to R^2=0.948 for the STD region.

The μFE strength ($\sigma_Y^{\mu FE}$) significantly decreased with the distal shift from STD to MD Region, and strength of the DS Region lay between the STD and the MD Regions. The decrease of the ultimate force was not found to be significant, but with the larger average cross sectional area at the MD Region, the decrease of the strength was significant. These findings go along with the results, observed for the apparent modulus, and could be explained the same way. Again, R^2 was higher for MD-DS comparison than for STD-DS comparison (MD: R^2=0.974; STD: R^2=0.933).

The differences between the regions showed that (see Tab. 3.1), all results for the MD region lay closer to the results for the DS region than those for the STD region. Also all correlation coefficients were higher for MD-DS than for STD-DS. This suggests that the damage occurs in the MD region, being included in the DS region than in the STD region.

There was no study available, to which the hFE results could be compared to, because the hFE modelling approach performed on distal radius sections was only published by Varga et.al. [36], but there, no hFE results of 9mm regions (STD & MD region) were reported. The resulting stiffnesses and from the hFE analysis (K^{hFE}) of the STD and MD regions did not significantly differ from those, obtained by the μFE analysis. Also the correlations (R^2, CC) between hFE and μFE stiffnesses were very good for both STD and MD regions (see Tab. 3.2). The hFE stiffness, different to the μFE stiffness, decreased significantly with the distal shift. These findings almost exactly reproduce the results reported by Varga et.al. [36]. The stiffness of the DS region was >50% lower than MD and STD stiffnesses, but as mentioned before, stiffnesses are, due to the different region dimensions, not comparable. Varga et.al. [36] reported also hFE stiffness of approximately 25kN/mm for the 20mm regions of the distal radius. Compared to the μFE results, the same observation could be made, despite the K^{hFE} lay now closer to the results for the 20mm regions.

The hFE derived ultimate forces (F_{ult}^{hFE}) were determined from a non-linear analysis, and therefore represent damage and yielding. F_{ult}^{hFE}, contrary to $F_{ult}^{\mu FE}$,

decreased with the distal shift. This might be explained by the actual fracture locations. Fractured domains are mostly included in the MD region and only a smaller part of them can be found within the STD region. The further decrease of the hFE ultimate force for the region extension to the DS region could result from the whole fracture, being included in the DS region. The hFE derived ultimate force was lower than F_{ult}^{hFE} reported by Varga (3.23±1.13kN).

The apparent modulus from the hFE calculations (E_{app}^{hFE}) decreased with the distal shift, just like the hFE derived stiffness, from which it was calculated from. As mentioned before, A_{avg} increased with the distal shift, and combined with the lower stiffness, the decrease in apparent modulus was significant. For the DS region, the apparent modulus further decreased, but this is clearly a result of the enlarged region length and, compared to the MD region, the decreased A_{avg} of the DS region. The hFE strength (σ_Y^{hFE}) was, as the ultimate force, lower for the MD region than for the STD region. Unlike the μFE strength, the hFE strength further decreased with the region extension to the DS region. This is contrary to what was expected and found for the μFE strength, but can be explained by the excessive decrease of F_{ult}^{hFE} from the STD or MD to the DS region. Comparable results could not be found in literature, because Varga et.al. [36] reported no apparent moduli and strengths. With the mean results from Varga, E_{app}^{hFE} resulted in 1459MPa and σ_Y^{hFE} in 9.3 MPa. These results were higher than the hFE results of the DS region.

In general, for the STD and MD regions, the hFE analysis resulted in higher ultimate forces and strengths than the μFE analysis. The DS results from the hFE analysis were again all consistently lower than the corresponding μFE results. Also the correlation coefficients between hFE and μFE were lower for the DS region than for STD and MD Regions.

4.2 Reproducibility and its Improvement through Image Registration

The choice to declare the first scan as the baseline was arbitrary and included the risk, that this measurement was an outlier. But in clinical evaluation there is also a first scan done and taken as the baseline for the following measurements, including the same risk.

When comparing the resulting reproducibility to results reported in literature, it has to be distinguished between *in vivo* and *in vitro* studies, because *in vivo*

studies include patient motion. Movement artefacts can have high effects on the reproducibility.

In general, only few data is available for comparing the reproducibility of HR-pQCT based bone mineral densities and even less for the reproducibility of HR-pQCT based FE analyses, as mainly the reproducibility of trabecular parameters are reported (e.g. [22], [24]).

4.2.1 Reproducibility of the Bone Density Measurements

To see, whether the baseline could be reproduced with the follow up, the baseline had to be compared to the follow up. The quality check QC1-Daily lay within the recommended range for the baseline scan and all five follow up scans. The HA density of the phantom showed a slight increase from the baseline to the 5th follow up. This increase could not be determined consistently in the BMC results of the STD regions. The mean±SD of the differences between BL and unregistered FU of both measurement and of the specimens (Tab. 3.5 horizontal and vertical, respectively) both included 0 in their 95%CI, so no significant change in the bone mineral density could be observed.

The STD region could be located throughout the follow up scans by a rather clear landmark. Therefore the STD region showed the smallest variances within the obtained bone mineral density results. The variation of the MD region was larger because the MostDistRefLin could not be located within the FU scans as well as the one for the STD regions. The number of slices, i.e. the height of the scanned region, was equal for STD and MD regions so the variation of the STD and MD results included only the variation of the variation of the positioning of the forearm within the scanner and the identification of the StdRefLin or MostDistRefLin. The variation of the results from the DS regions additionally included the variation of the region height, i.e. the variation of the determined location of the StdRefLin and MostDistRegLin. The height for the DS regions varied for the unregistered follow up scans, e.g. between 12.5mm and 15.3mm for the specimen C_M_1938_R.

The precision errors $PE_{\%CV}$ and their 95%CI for the bone mineral density measures BMC, vBMD and aBMD were higher for the MD regions than for the STD regions: 1.5% to 3% for MD compared to 1% to 2% for STD. For the DS regions the precision errors of BMC, vBMD and aBMD were higher than those for STD or MD, 4% to 4.5% for the STD regions. $PE_{\%CV}$ of aBMD and vBMD included the errors of BMC, and were higher. Similar results were found in a

previous study by Boutroy et.al. [6], who reported a $PE_{\%CV}$ for vBMD of 0.9% for 3 consecutive *in vivo* measurements of 15 individuals. The precision error from this study included motion, but was still lower, compared to the obtained results in the present study. This might be a result of the lower number of repeated measurements (3 compared to 6) and the fact that the individual's measured aged from 21-47yrs. All ICCs of BMC, vBMD and aBMD showed a high reproducibility (>0.99) for STD and MD regions. The high ICC do not solely result from the precision of the measurement but also from the high between-subject-variance. Similar results for slightly different regions were reported by Müller et.al. [24]. The ICCs for the bone mineral density measures of the DS regions were lower, but still above 0.96.

Image registration was able to decrease the $PE_{\%CV}$ of BMC, vBMD and aBMD for the STD, MD and DS regions. The precision errors now ranged from 0.4% to 1.4% and 0.5% to 1.2% for the STD and MD regions, respectively. Due to the chosen image registration method, preserving the $GreySum$ within the image during the registration the baseline results did not differ from the registered FU results. These results are similar to those, reported by MacNeil et.al. [22] for a *in vivo* analysis: $PE_{\%CV}$ for vBMD 0.4%. The lower error might be a result of the higher number of specimens (N=30) and the fact that the ages of the individuals were 20 to 40 years. The decrease of the precision errors lay in a range of 80% for vBMD, 60% for BMC and below 20% for aBMD. For the DS regions the precision errors for BMC, vBMD and aBMD showed a greater decrease after image registration and the final precision errors were similar to those from the MD region ($PE_{\%CV}$ from 0.5% to 1.7%). The decrease of vBMD lay still in the same range, compared to STD or MD regions, whereas the decreases for BMC and aBMD were larger. This also comes from the fact that the variation of the unregistered FU included, next to the variation of location, the variation of the region heights. This effect of variation of the region heights was removed by the image registration. This contributes to the larger decrease of the precision error. The image registration also increased the ICCs, determined for BMC, vBMD and aBMD for the STD, MD and DS regions to 0.994 to 1.000. Similarly, as observed for precision errors, the increase of ICC for aBMD was lower for STD and MD regions than for BMC and vBMD in these regions. The increase of aBMD ICC for the DS Regions also increased, but mostly due to the constant region height within the registered DS FU images.

4.2.2 Reproducibility of the FE-Analysis

The mean±SD of the differences between BL and unregistered FU μFE and hFE results also included 0 in their 95%CI. Thus the μFE and hFE modelling approaches do not induce additional variability or a shift of the results.

$PE_{\%CV}$ were again higher for MD than for STD regions: 3.0% to 4.1% compared to 1.2% to 3.3%. In general, these values are slightly higher than those for the bone mineral density measures. Müller et.al. reported similar precision errors for $K^{\mu FE}$ of 2.9% and 1.2% for the two regions, representing the MD and STD regions analysed in the present study [24]. For the STD and MD regions, the reproducibility of the *structural* FE measures (K and F_{ult}) was higher, i.e. lower $PE_{\%CV}$s, than the reproducibility for the *material* FE measures (E_{app} and σ_Y). This was also observed for the bone mineral density measures. This might be explained through the definition of E_{app} and σ_Y in the present study. The division through the varying average cross-sectional area (A_{avg}) introduces additional variability for these two results. For the DS regions the precision errors of the μFE results were higher than those for STD or MD regions, 2.1% to 5.6%. The hFE results for the DS regions were not calculated.

The ICCs of the μFE results were higher for *structural* FE measures than for the *material* FE measures for STD, MD and DS regions. Also the reproducibility was higher for the μFE results than for the hFE results for all regions. In general the FE-results of both μFE and hFE analyses of the STD region was most reproducible, already at the unregistered stage (μFE: >0.992, hFE: >0.982). The FE results of the DS region were least reproducible, except for the ultimate force (ICC=0.995). The high ICC were again not solely a product of the low measurement variance but resulted also from the high between subject variance, e.g. for STD baseline $K^{\mu FE}$ ranged from 50kN/mm to 117kN/mm.

The mean±SD of the differences between BL and registered FU of the μFE and hFE results showed systematic shifts: μFE decreased and hFE increased after the image registration. The decrease for the μFE results could be explained with a loss of elements after the segmentation of the registered follow up images (mean loss of elements: STD: 0.5%; MD: 1.0%; DS: 1.0%). These losses were most probably introduced by partial volume effects, resulting from the re-sampling after the image registration. These losses may represent a lower bone volume fraction and structural connectivity within the registered μFE models.

One possible explanation for the increase of the hFE results might have been a result from an increase in cortical BMC (Ct.BMC) and cortical volume (Ct.Vol) of

4.5% and 9%, respectively. The discrepancies between the 9% increase of Ct.Vol and ∼4% of hFE measures come from the fact that the cortical orthotropy is aligned to the geometry of the cortex, which itself is not aligned with the loading direction. The fabric evaluation from the segmented registered FU images and the BV/TV^d evaluation were not affected by the registration.

The precision errors could be decreased through the image registration by 40% to 80% to final values of 0.7% to 0.8%, 1.0% to 2.4% and 1.2% to 1.4% for the STD, MD and DS regions, respectively. MacNeil et.al. [22] reported precision errors of 1.4% to 2.4% for the apparent modulus and the reaction force of the STD region, induced by 1% strain from uni-axial displacement, after image registration by a 2D area matching method. The reproducibility of this reaction force is comparable to the reproducibility of the stiffness in the present study. Here the reaction force, induced by 0.1mm uni-axial displacement (=1.1% uni-axial strain), was just divided by this displacement to get the apparent stiffness. The precision errors of the apparent modulus and the reaction force there, were higher than those, found in the present study. With a 3D image registration method, MacNeil et.al. could improve the reproducibility of the structural trabecular parameters and the bone mineral density. It was not reported, whether these improvements could also be observed for the mechanical properties [22].

For the STD region the ICCs of both μFE and hFE results could be raised to 0.999 - 1.000 through the image registration. For the MD and the DS region, the ICCs could also be increased to 0.991 - 0.999 and 0.998 - 0.998, respectively. The increase for the DS region was again highest, due to the equalized region dimensions after the registration. These ICCs were comparable to the values, reported by Müller et.al., who also used the 2D-area matching method: 0.998 to 0.999 for μFE stiffness and ultimate force.

4.3 Limitations

The most limiting factor in the presented study is the fact that patient motion is <u>not</u> included. Motion artefacts will worsen the reproducibility, i.e. increase $PE_{\%CV}$ and decrease ICC. FE results will be more affected than the bone mineral density evaluation and, due to the homogenization, hFE will be more robust to motion artefacts than μFE results. The μFE models rely on an intact cortical shell and trabecular architecture. The observed precision errors and LSC were at the lower bound of results, found in literature for *in vivo* studies, as only the

repositioning errors and the machine errors, reported to be <0.3% by MacNeil et.al. [22], were included in this study. The results of the present study also represent, due to the age of the specimens and the lower amount of trabecular bone in elderly specimens, the upper bound of the reproducibility errors.

Some details of the methods, described in Chapter 2, and their contribution to the reproducibility are discussed in the following.

As a result of the dissection at the elbow, the ulna and the radius were no longer restricted in relative motion at their proximal epiphysis within the forearm. This might have also influenced the reproducibility. Problems with this point were observed with the four largest (male) specimens. Due to their size, especially the big circumference of the forearm at the proximal end (elbow), the radius and the ulna could move within the soft tissue (muscles, tendons, vascular system, ...). Within some scans of the above mentioned specimens, this lead to a non parallel positioning of radius and ulna. The orientation of the radius was no longer parallel to the standard forearm fixation, which does not correspond to the *in vivo* situation.

The choice to take the same homogeneous material properties for both cortical and trabecular elements in the μFE analysis was not thought to have a major impact on the reproducibility. With a variation of the cortical thickness, different material properties for cortical elements (e.g. see [7], [37]) will probably still effect the reproducibility of the μFE-results, but this effect was not investigated within the present study.

The framework for the automated hFE analysis [26] is currently not completely finished for the analysis of the distal radius. In opposite to the μFE analysis, which could be completely automated and had only few parameters to be set, the hFE modelling requires still high operator interaction. The advantage of the hFE was that all calculations could be performed with comparatively low computational effort, e.g. on a desktop computer. So far, the weakest point of the framework, observed in the present study, was the creation of the iso-surfaces. For the *fill* algorithm a global threshold must be set to identify the outer and inner cortex contour. With a slightly varying image quality it was not possible to create smooth inner cortex contours for all models. In the present study, and also in previous studies (e.g. [36]), the triangulated 2D surface meshes had to be corrected in a pre-processor. This was very time consuming, for the BL unregistered FU, each and every mesh had to be checked, and if necessary, corrected. This resulted in 6x12x2=144 meshes from baseline and 5 follow ups, 12 specimens and 2 regions

(STD & MD) and another 12 meshes from the DS baseline. This was also a reason for not analysing the unregistered hFE FU for the DS Region. Another 60 meshes would have contributed to the work going beyond the scheduled amount. The extension and cropping of the 'inner' and 'thickness' masks for the FU images of the DS regions was another task, limiting the hFE analysis of the DS region to the baseline.

Another task limiting this study was the definition of the DS regions. The DS regions in this study were cropped from images of two adjacent 9mm regions, which were scanned at once. To limit motion artefacts, the patient will be allowed to move between these two scans. Therefore the adjacent 9m regions will have to be scanned with an overlap. The overlapping parts of these regions can be used for image registration, to construct the DS regions.

4.4 Outlook and Future Prospectives

An *in vivo* study on volunteer patients is at risk to include movement artefacts. The reproducibility of an *in vivo* study will therefore lead to clinically relevant values of the *in vivo* reproducibility. It will be also possible to scan younger patients with more intact bone geometry and trabecular architecture.

The systematic shifts of both μFE and hFE results after the image registration need to be investigated more deeply. The suggestions, for the reasons of the increase of μFE as well for the decrease of hFE presented in this study, need to be confirmed.

The reproducibility of hFE analysis of the unregistered and registered follow up of the DS region needs to be investigated, to see whether the reproducibility ($PE_{\%CV}$, ICC) is similar to DS μFE and if the reproducibility after the image registration can also be improved. Additionally the results should also be checked for the systematic increase after the image registration.

4.5 Conclusions

The modelling strategies, used in the present study, lead to reasonable results for both μFE and hFE analyses. The reproducibility, quantified by precision errors and ICC, was already high for the unregistered follow up bone mineral density results and FE-results. The reproducibility was: highest for the STD region, followed by the MD and the DS region, and in general higher for the bone mineral

density measures than for the FE-results.

Image registration could improve the reproducibility. The reproducibility of the results of the DS regions could be most improved by the image registration, due to the equalized region heights. The image registration induced a systematic shift of both μFE and hFE results, a decrease of μFE and an increase of hFE results.

List of Symbols

2D	2 dimensional
3D	3 dimensional
A_{avg}	Average cross-sectional area of the regions
A_{proj}	dorsal-palmar projected area of the regions
BL	Baseline
BMC	Bone Mineral Content
BMD	Bone Mineral Density
aBMD	areal Bone Mineral Density
vBMD	volumetric Bone Mineral Density
BSV	Between-subject-variance
BV/TV	Bone Volume to Total Volume
BV/TV^{d}	Density based BV/TV
CI	Confidence Interval
CT	Computed Tomography
%CV	Coefficient of Variance
D	Distance between StdRefLin and MostDistRefLin
D	Damage variable
Diff	Difference between Baseline and Follow Up
DS	Double Section Region
DXA	Dual X-Ray Energy Densitometry
$\mathbf{E}$	2nd order Green-StVernant strain tensor
$\mathbf{E}^P$	plastic part of $\mathbf{E}$
$\mathbb{E}$	4th order compliance tensor
E_{app}^{hFE}	hFE derived apparent modulus
$E_{app}^{\mu FE}$	μFE derived apparent modulus
$\mathbf{F}$	nodal forces
F_{ult}^{hFE}	μFE derived ultimate force
$F_{ult}^{\mu FE}$	hFE derived ultimate force
FE	Finite Element
FU	Follow Up
G_0	shear modulus
GOBJ	Graphical Object
GreySum	Grey-value sum within the CT-images
h	height of the regions
HA	Hydroxyapatite
hFE	homogenized Finite Element
HR-pQCT	High Resolution peripheral QCT

ICC	Interclass Correlation
k	density power coefficient
$\mathbf{K}$	global stiffness matrix
K^{hFE}	hFE derived stiffness
$K^{\mu FE}$	μFE derived stiffness
l	fabric power coefficient
L95	lower border of ICC 95%CI
LSC	Least Significant Change
$\mathbf{M}$	2nd order fabric tensor
m_i	eigenvalues of $\mathbf{M}$
$\mathbf{m_i}$	eigenvectors $\mathbf{M}$
MD	Most Distal Region
MIL	Mean Intercept Length
MostDistRefLin	Most Distal Reference Line
MS_{BONE}	Normalized Mean Squares Metric
MS_{TOT}	Mean Squares Metric
N_{BONE}	total number of bone voxels within the image
N_{TOT}	total number of voxels within the image
ODF	Orientation Distribution Function
$PE_{\%CV}$	Precision Error of %CV
PE_{SD}	Precision Error of SD
QCT	Quantitative Computed Tomography
$r^D(D)$	damage evolution function
$\mathbf{S}$	2nd order PK2 stress tensor
$\mathbf{S}^D$	damage stress tensor
$\mathbf{S}^P$	plastic part of $\mathbf{S}$
SD	standard deviation
STD	Standard Region
StdRefLin	Standard Reference Line
$\mathbf{U}$	nodal displacements
U95	upper border of ICC 95%CI
V_{BONE}	bone volume
VOI	volume of interest
WSV	within-subject-variance
$\overline{X}$	overall mean
$\overline{X_j}$	specimen mean
XCT	XtremeCT
Y^P	damage threshold function
Y^P	plastic yield threshold function
ϵ_0	Young' Modulus
μ	X-Ray attenuation coefficient
μFE	micro Finite Element
μCT	micro CT
ν	Poisson's Ratio
ρ	volume fraction
σ^P	hardening function
σ_Y^{hFE}	hFE derived apparent strength
$\sigma_Y^{\mu FE}$	μFE derived apparent strength

Bibliography

[1] Assessment of fracture risk and its application to screening for postmenopausal osteoporosis. report of a who study group. *World Health Organ Tech Rep Ser*, 843:1–129, 1994.

[2] *XtremeCT Manual, Scanco Mecical AG*, 2007.

[3] J. E. Adams. Quantitative computed tomography. *Eur J Radiol*, 71(3):415–424, Sep 2009.

[4] P. Arbenz, G. van Lenthe, U. Mennel, R. Müller, and M. Sala. A scalable multi-level preconditioner for matrix-free u-finite element analysis of human bone structures. *Int J Num Method Eng*, 73:927–947, 2008.

[5] K. Bathe. *Finite Element Procedures.* Prentice Hall, 1995.

[6] S. Boutroy, M. L. Bouxsein, F. Munoz, and P. D. Delmas. In vivo assessment of trabecular bone microarchitecture by high-resolution peripheral quantitative computed tomography. *J Clin Endocrinol Metab*, 90(12):6508–6515, Dec 2005.

[7] S. Boutroy, B. V. Rietbergen, E. Sornay-Rendu, F. Munoz, M. L. Bouxsein, and P. D. Delmas. Finite element analysis based on in vivo hr-pqct images of the distal radius is associated with wrist fracture in postmenopausal women. *J Bone Miner Res*, 23(3):392–399, Mar 2008.

[8] H. Buie, G. Campell, R. Klinck, J. MacNeil, and S. Boyd. Automatic segmentation of cortical and trabecular compartments based on a dual thresold technique for in vivo micro-ct bone analysis. *Bone*, 41:505–515, 2007.

[9] A. Burghardt, R. Buie, A. Laib, S. Majumdar, and S. Boyd. Reproducibility of direct quantitative measures of cortical bone microarchitecture of the distal radius and tibia by hr-pqct. *Bone*, -:–, 2010.

[10] A. J. Burghardt, G. J. Kazakia, T. M. Link, and S. Majumdar. Automated simulation of areal bone mineral density assessment in the distal radius from high-resolution peripheral quantitative computed tomography. *Osteoporos Int*, 20(12):2017–2024, Dec 2009.

[11] R. Eastell, H. Wahner, W. O'Fallon, P. Amadio, L. Melton, and B. Riggs. Unequal decrease in bone density of lumbar spine and ultradistal radius in colles' and vertebral fracture syndromes. *J Clin Invest*, 83:168–174, 1989.

[12] D. Garcia, P. K. Zysset, M. Charlebois, and A. Curnier. A three-dimensional elastic plastic damage constitutive law for bone tissue. *Biomech Model Mechanobiol*, 8(2):149–165, Apr 2009.

[13] C. Geuzaine and J. Remacle. Gmsh: a three-dimensional finite element mesh generator with built-in and pre- and post-processing facilities. *Int J Num Method Eng*, 79:1309–1331, 2009.

[14] G.N. Hounsfield Computed medical imaging. *Med Phys*, 7:283, 1980.

[15] H. Gray. *Anatomy of the human body.* Lea&Febiger; bartleby.com, 1918; 2000.

[16] K. Gwet. Intrarater reliability. Technical report, STATAXIS Consulting, 2008.

[17] R. Hannon, A. Blumsohn, K. Naylor, and R. Eastell. Response to biochemical markers of bone turnover to hormone replacement therapy: Impact of biological variability. *J Bone Min Res*, 13:1124–1133, 1998.

[18] J. Homminga, R. Huiskes, B. van Rietbergen, P. Ruegsegger, and H. Weinans. Introduction and evaluation of a gray-value voxel conversion technique. *J Biomech*, 34:513–517, 2001.

[19] T. Kohler, M. Beyeler, D. Webster, and R. M"uller. Compartmental bone morphometry in the mouse femur: reproducibility and resolution dependence of microtomographic measurements. *Calcif Tissue Int*, 77(5):281–290, Nov 2005.

[20] A. Laib, H. Huselmann, and P. Rüegsegger. In vivo high resolution 3d-qct of the human forearm. *Technol Health Care*, 6:329–337, 1998.

[21] A. Laib and P. Rüegsegger. Comparison of structure extraction methods for in vivo trabecular bone measurements. *Comput Med Imaging Graph*, 23(2):69–74, 1999.

[22] J. A. Macneil and S. K. Boyd. Bone strength at the distal radius can be estimated from high-resolution peripheral quantitative computed tomography and the finite element method. *Bone*, 42(6):1203–1213, Jun 2008.

[23] G. Mazza, G. Franzoso, M. Pretterklieber, and P. Zysset. Anisotropic elastic properties of vertebral compact bone measured by microindentation. *Journal of Biomechanics*, 41:S75, 2008.

[24] T. Müller, M. Stauber, T. Kohler, F. Eckstein, R. Müller, and G. van Lenthe. Non-invasive bone competence analysis by high-resolution pqct: An in vitro reproducibility study on structural and mechanical properties at the human radius. *Bone*, 44:364–371, 2009.

[25] K. K. Nishiyama, G. M. Campbell, R. J. Klinck, and S. K. Boyd. Reproducibility of bone micro-architecture measurements in rodents by in vivo micro-computed tomography is maximized with three-dimensional image registration. *Bone*, 46(1):155–161, Jan 2010.

[26] D. H. Pahr and P. K. Zysset. From high-resolution ct data to finite element models: development of an integrated modular framework. *Comput Methods Biomech Biomed Engin*, 12(1):45–57, Feb 2009.

[27] W. Pistoia, B. van Rietbergen, E.-M. Lochmüller, C. A. Lill, F. Eckstein, and P. Rüegsegger. Estimation of distal radius failure load with micro-finite element analysis models based on three-dimensional peripheral quantitative computed tomography images. *Bone*, 30(6):842–848, Jun 2002.

[28] M. Read. Osteoporosis in the european community: Action plan. Technical report, European Union Osteoporosis Consultation Panel, 2002.

[29] J. Y. Rho, L. Kuhn-Spearing, and P. Zioupos. Mechanical properties and the hierarchical structure of bone. *Med Eng Phys*, 20(2):92–102, Mar 1998.

[30] T. Ridler and S. Calvard. Picture thresholding using an iterative selection method. *IEEE Trans Syst Man Cyb*, 8:630–632, 1978.

[31] L. Rincon-Kohli and P. K. Zysset. Multi-axial mechanical properties of human trabecular bone. *Biomech Model Mechanobiol*, 8(3):195–208, Jun 2009.

[32] P. Shrout. Intraclass correlations: uses in assessing rater reliability. *Psychiol Bull*, 86:420–428, 1979.

[33] J. Spadaro, F. Werner, R. Brenner, M. Fortino, L. Fay, and W. Edwards. Cortical and trabecular bone contribute strength to the osteopenic distal radius. *J Orthop Res*, 12:211–218, 1994.

[34] G. Treece, R. Prager, A. Gee, and L. Berman. Surface interpolation from sparse cross-sections using region correspondence. *IEEE Trans Med Imag*, 19:1106–1114, 2000.

[35] B. van Rietbergen, H. Weinans, R. Huiskes, and A. Odgaard. A new method to determine trabecular bone elastic properties and loading using micromechanical finite-element models. *J Biomech*, 28(1):69–81, Jan 1995.

[36] P. Varga. *Prediction of Distal Radius Fracture Load Using HR-pQCT-based Finite Element Analysis*. PhD thesis, Vienna University of Technology, 2009.

[37] N. Vilayphiou, S. Boutroy, E. Sornay-Rendu, B. V. Rietbergen, F. Munoz, P. D. Delmas, and R. Chapurlat. Finite element analysis performed on radius and tibia hr-pqct images and fragility fractures at all sites in postmenopausal women. *Bone*, 46(4):1030–1037, Apr 2010.

[38] W. Whitehouse. The quantitative morphology of anisotropic trabecular bone. *J Microsc*, 101:153–168, 1974.

[39] P. K. Zysset. A review of morphology-elasticity relationships in human trabecular bone: theories and experiments. *J Biomech*, 36(10):1469–1485, Oct 2003.

[40] P. K. Zysset and A. Curnier. A 3d damage model for trabecular bone based on fabric tensors. *J Biomech*, 29(12):1549–1558, Dec 1996.